A Three-Phase Model for Mixed Columnar-Equiaxed Solidification

MENGHUAI WU and ANDREAS LUDWIG

A three-phase model for mixed columnar-equiaxed solidification is presented in this article. The three phases are the parent melt as the primary phase, as well as the solidifying columnar dendrites and globular equiaxed grains as two different secondary phases. With an Eulerian approach, the three phases are considered as spatially coupled and interpenetrating continua. The conservation equations of mass, momentum, species, and enthalpy are solved for all three phases. An additional conservation equation for the number density of the equiaxed grains is defined and solved. Nucleation of the equiaxed grains, diffusion-controlled growth of both columnar and equiaxed phases, interphase exchanges, and interactions such as mass transfer during solidification, drag force, solute partitioning at the liquid/solid interface, and release of latent heat are taken into account. Binary steel ingots (Fe-0.34 wt pct C) with two-dimensional (2-D) axis symmetrical and three-dimensional (3-D) geometries as a benchmark were simulated. It is demonstrated that the model can be used to simulate the mixed columnar-equiaxed solidification, including melt convection and grain sedimentation, macrosegregation, columnar-to-equiaxed-transition (CET), and macrostructure distribution. The model was evaluated by comparing it to classical analytical models based on limited one-dimensional (1-D) cases. Satisfactory results were obtained. It is also shown that in order to apply this model for industrial castings, further improvements are still necessary concerning some details.

I. INTRODUCTION

THERE are two typical macrostructures in metal castings: columnar dendrites and equiaxed grains. To model mixed columnar-equiaxed solidification, it is necessary to consider the competitive growth of the columnar dendrites and the equiaxed grains in combination with melt convection and grain transport. An important feature in describing the mixed columnar-equiaxed solidification is the so-called columnar-to-equiaxed-transition (CET), to which great attention has been paid in the last decades.[1–5] A widespread opinion is that the CET is induced by the competitive growth of the columnar dendrites and equiaxed grains, and thus, most research work has been focused on this. The columnar tips are either blocked mechanically by the presence of equiaxed grains ahead of the columnar front, which is known as the ''hard-blocking'' mechanism,[1] or they are blocked by the disappearance of local constitutional undercooling, which is known as the ''soft-blocking'' mechanism.[4,5] Although the role of melt convection and grain transport in macrostructure formation has since long been known,[6] the study of grain transport and its influence on the CET is unfortunately very rare.[3]

Obviously, mixed columnar-equiaxed solidification is a typical multiphase problem. This article reports about the extension of a two-phase model for describing the equiaxed globular solidification published earlier by the authors,[7,8] to a three-phase model by including an additional columnar phase. Both the columnar-equiaxed competitive growth and the grain rearrangement due to movement of the equiaxed grains are taken into account. The origin of the equiaxed grains is thought to be heterogeneous nucleation. Dendrite fragmentation, although sometimes believed to play an important role in the mixed columnar-equiaxed solidification, is not included.

Simulation results for a binary steel benchmark ingot (Fe-0.34 wt pct C) with a two dimensional (2-D) axis symmetrical and a three-dimensional (3-D) geometry are presented to demonstrate the potential of the model. Additionally, some one-dimensional (1-D) cases are simulated and evaluated by comparing them to classical analytical solutions. The limitations of the recent model and necessary further improvements are also discussed.

II. MODEL DESCRIPTION

A. *General Assumptions*

(1) Three phases are defined: the primary liquid phase (l), the equiaxed phase as the first secondary phase (e), and the columnar as the second secondary phase (c). The corresponding phase fraction is given by f_l, f_e, and f_c with $f_l + f_e + f_c = 1$. Both the primary and equiaxed phases are moving phases, for which the corresponding Navier–Stokes equations are solved. The columnar phase is assumed to stick to the wall and solidify from the wall toward the bulk melt. Thus, no momentum equation for the columnar phase is considered, (2) Ideal morphologies for both solid phases are assumed: spheres for equiaxed (globular) grains and cylinders for columnar (cellular) dendrites, (3) The grain size of equiaxed grains and the diameter of the columnar trunks are explicitly calculated, while a constant value for the primary arm spacing of columnar dendrites is assumed, (4) No feeding flow is included (except in Section V–B). The Boussinesq approach is employed to model thermosolutal convection, grain sedimentation, and sedimentation-induced melt convection, and (5) Grain fragments brought

---

MENGHUAI WU, Group Leader of Numerical Modeling and Simulation, and ANDREAS LUDWIG, Professor and Director, are with Simulation and Modeling of Metallurgical Processes, Christian-Doppler-Laboratory for Multiphase Modeling of Metallurgical Processes, Department of Metallurgy, University of Leoben, A8700 Leoben, Austria. Contact e-mail: menghuai.wu@notes.unileoben.ac.at

Manuscript submitted March 13, 2005.

into the mold during filling and further fragmentation of dendrites during growth are not modeled.

B. *Nucleation of the Equiaxed Grains and Grain Transport*

The number density of equiaxed grains, n, is calculated by the conservation equation:

$$\frac{\partial}{\partial t} n + \nabla \cdot (\mathbf{u}_e n) = N_e \qquad [1]$$

Here, $\mathbf{u}_e$ is the volume-averaged velocity of the equiaxed phase. The nucleation rate, N_e, has the unit $\mathrm{m}^{-3} \cdot \mathrm{s}^{-1}$. A three-parameter heterogeneous nucleation law[7,9] is used to define the source term:

$$N_e = \frac{dn}{dt} = \frac{dn}{d(\Delta T)} \cdot \frac{d(\Delta T)}{dt} = \frac{d(\Delta T)}{dt} \cdot \frac{n_{\max}}{\sqrt{2\pi} \cdot \Delta T_\sigma} \cdot e^{-\frac{1}{2}\left(\frac{\Delta T - \Delta T_N}{\Delta T_\sigma}\right)^2} \qquad [2]$$

where $\Delta T = T_f + mc_l - T$ is the constitutional undercooling, with T_f being the melting point of the major constituent, m the liquidus slope, and c_l the volume-averaged liquid concentration. The three nucleation parameters (ΔT_N, $n_{\max}$, and ΔT_σ) must be determined experimentally.[9]

C. *Mass Conservation and Grain Growth Kinetics*

The mass conservation equations are

$$\frac{\partial}{\partial t}(f_l \rho_l) + \nabla \cdot (f_l \rho_l \mathbf{u}_l) = M_{el} + M_{cl} \qquad [3]$$

$$\frac{\partial}{\partial f}(f_e \rho_e) + \nabla \cdot (f_e \rho_e \mathbf{u}_e) = M_{le} + M_{ce} \qquad [4]$$

$$\frac{\partial}{\partial t}(f_c \rho_c) + \nabla \cdot (f_c \rho_c \mathbf{u}_c) = M_{lc} + M_{ec} \qquad [5]$$

Here, ρ_l, ρ_e, and ρ_c are the densities and $\mathbf{u}_l$, $\mathbf{u}_e$, and $\mathbf{u}_c$ are the volume-averaged velocities of the different phases. The source terms represent the net mass-transfer rates (kg/m^3/s), where $M_{lc}(= -M_{cl})$ is from the liquid to the columnar phase, $M_{le}(= -M_{el})$ is from the liquid to the equiaxed phase by solidification (positive) or melting (negative), and $M_{ce}(= -M_{ec})$ is from the columnar to the equiaxed phase by the mechanism of fragmentation (positive) or of attaching (negative). Melting of the solid phases can also be taken into account,[7] but the simulation results presented in this article did not do so. As already mentioned previously, fragmentation and attachment are ignored, so we chose $M_{ce} = 0$.

For the Eulerian multiphase calculations, the phase-coupled SIMPLE (extended) algorithm is used for the pressure-velocity coupling. An additional pressure correction equation is built based on total volume continuity.[10] Accordingly, pressure and velocities are corrected to satisfy this continuity constraint. The volume fraction of the secondary phases f_e and f_c are explicitly calculated *via* Eqs. [4] and [5]; the volume fraction of the primary phase f_l is obtained by the relationship $f_l + f_e + f_c = 1$.

In order to define the net mass-transfer rate, diffusion-controlled grain growth kinetics on the microscale must be modeled. As mentioned previously, we assume an ideal spherical morphology for equiaxed solidification. Therefore, the grain growth velocity in the radius direction, v_{R_e}, can be solved analytically[11] to give

$$v_{R_e} = \frac{dR_e}{dt} = \frac{D_l}{R_e} \cdot \frac{c_l^* - c_l}{c_l^* - c_s^*} = \frac{D_l}{R_e(1-k)} \cdot \left(1 - \frac{c_l}{c_l^*}\right) \qquad [6]$$

Here, c_l^* and c_s^* are the equilibrium liquid and solid concentrations adjacent to the solid/liquid interface, for which $c_s^* = kc_l^*$ (with a constant redistribution coefficient k) and $c_l^* = (T - T_f)/m$ yields. The term D_l is the diffusion coefficient in the liquid. The volume-averaged radius of equiaxed grains, $R_e = d_e/2$, is calculated according to the relationship between the volume fraction of the equiaxed phase, f_e, and the volume-averaged number density of the equiaxed grains, n, as described in Section G. With Eq. [6], we can define the volume-averaged net mass-transfer rate for globular equiaxed solidification by considering the total surface area of spherical grains and taking the impingement by an Avrami-factor f_l into account. So, we obtain

$$M_{le} = v_{Re} \cdot \left(n \cdot \pi d_e^2\right) \cdot \rho_e \cdot f_l \qquad [7]$$

and with Eq. [6],

$$M_{le} = \frac{D_l}{(d_e/2) \cdot (1-k)} \cdot \left(1 - \frac{c_l}{(T - T_f)/m}\right) \cdot \left(n \cdot \pi d_e^2\right) \cdot \rho_e \cdot f_l \qquad [8]$$

For columnar solidification, the columnar dendrites are approximated by growing cylinders, which reveal an average distance given by the primary arm spacing, λ_1. For defining the net mass-transfer rate, we distinguish between (1) the tip regions, (2) the bulk melts ahead of the tips, and (3) the growing columnar trunks. We trace the tip front of the columnar dendrites by a method described in Section H. For the volume elements that have not yet been reached by the columnar tip front, we chose $M_{lc} \equiv 0$. For the volume elements that have already been pasted by the tip front, a diffusion-controlled growth model around the cylindrical dendrite trunks is used. Similar to the growth of spherical grains, the growth velocity in the radial direction of such a cylindrical trunk is thus

$$v_{R_e} = \frac{dR_c}{dt} = \frac{D_l}{R_c} \cdot \frac{c_l^* - c_l}{c_l^* - c_s^*} \ln^{-1}\left(\frac{R_f}{R_c}\right) \qquad [9]$$

where $R_c = d_c/2$ is the average radius of a cylindrical dendrite trunk, and $R_f = \lambda_1/2$ is half of the primary arm spacing, λ_1. So, we can define the volume-averaged net mass-transfer rate for those volume elements by considering the total surface area of columnar dendrite trunks per volume $S_A = \pi d_c/\lambda_1^2$, and an Avrami-factor f_l to become

$$M_{lc} = v_{R_e} \cdot \left(\pi d_c/\lambda_1^2\right) \cdot \rho_c \cdot f_l \qquad [10]$$

and with Eq. [9],

$$M_{lc} = \frac{D_l}{(d_c/2)\cdot(1-k)}\cdot\left(1-\frac{c_l}{(T-T_f)/m}\right)\cdot \ln^{-1}\left(\frac{\lambda_1}{d_c}\right)\cdot(\pi d_c/\lambda_1^2)\cdot\rho_c\cdot f_l \qquad [11]$$

For the elements containing growing columnar tips, the mass-transfer rate M_{lc} for columnar solidification is written by taking both the tip growth velocity v_{tip} and the radial growth velocity v_{R_c} into account.

$$M_{lc} = v_{R_c}\cdot n_c\cdot(\pi d_c\cdot l)\cdot\rho_l\cdot f_l + v_{\mathrm{tip}}\cdot n_c\cdot\left(\pi R_{\mathrm{tip}}^2\right)\cdot\rho_l\cdot f_l \qquad [12]$$

The actual columnar length l is calculated in Section H. The first term on the left side of Eq. [12] denotes the net mass-transfer rate due to growth in the radial direction, and the second term that of growth in the axial direction, $n_c = 4f_c/\left(\pi d_c^2\cdot l\right)$ is the number density of columnar trunks. The dendrite tip velocity v_{tip} and the tip radius R_{tip} are calculated according to References 11 and 12.

D. *Momentum Conservation and Viscous Interaction between Phases*

The velocity fields of the parent melt and the moving equiaxed phase are obtained by solving the Navier–Stokes equations:

$$\frac{\partial}{\partial t}(f_l\rho_l\mathbf{u}_l) + \nabla\cdot(f_l\rho_l\mathbf{u}_l\otimes\mathbf{u}_l) = -f_l\nabla p + \nabla\cdot\overline{\overline{\tau}}_l + \mathbf{F}_{Bl} + \mathbf{U}_{cl} + \mathbf{U}_{el} + \mathbf{F}_l^s \qquad [13]$$

$$\frac{\partial}{\partial t}(f_e\rho_e\mathbf{u}_e) + \nabla\cdot(f_e\rho_e\mathbf{u}_e\otimes\mathbf{u}_e) = -f_e\nabla p + \nabla\cdot\overline{\overline{\tau}}_e + \mathbf{F}_{Be} + \mathbf{U}_{le} + \mathbf{U}_{ce} + \mathbf{F}_e^s \qquad [14]$$

with $\overline{\overline{\tau}}_l = \mu_l f_l\left(\nabla\otimes\mathbf{u}_l + (\nabla\otimes\mathbf{u}_l)^T\right)$ being the stress-strain tensor of the liquid phase and $\overline{\overline{\tau}}_e = \mu_e f_e\left(\nabla\otimes\mathbf{u}_e + (\nabla\otimes\mathbf{u}_e)^T\right)$ that of the equiaxed phase. The term μ_e is the viscosity of the equiaxed phase defined in Reference 7.

With the Boussinesq approach, the buoyancy force for the free moving grains is defined as

$$\mathbf{F}_{Be} = f_e\cdot\rho\cdot\mathbf{g}_e' \text{ with } \mathbf{g}_e' = \frac{\Delta\rho}{\rho}\mathbf{g} = \frac{\rho_e-\rho_l}{\rho}\mathbf{g} \qquad [15]$$

and the thermosolutal buoyancy force is defined as

$$\mathbf{F}_{Bl} = f_l\cdot\rho\cdot\mathbf{g}_l' \text{ with } \mathbf{g}_l' = \frac{\Delta_\rho}{\rho}\mathbf{g} = \frac{\rho_l(T,c)-\rho_l^{\mathrm{ref}}}{\rho}\mathbf{g}$$
$$\text{and } \rho_l(T,c) = \rho_l^{\mathrm{ref}}\cdot\ \ 1+\beta_T\cdot(T^{\mathrm{ref}}-T_l+\beta_c\cdot(c^{\mathrm{ref}}-c_l) \qquad [16]$$

Additional forces, $\mathbf{F}_l^s$ and $\mathbf{F}_e^s$, can be added to the equations, but are not considered in this article. All other momentum exchange terms are summarized in Table I. Details concerning these exchange terms were described in former publications by the authors.[7,8] One point that needs to be mentioned is that a rather simple model for the interaction between the columnar and the equiaxed phase is used. We assume that when the local volume fraction of the columnar phase is more than a critical value (($f_c^{\mathrm{free}} = 0.2$), an infinite drag force coefficient between both solid phases can be applied. However, when the volume fraction of the columnar phase is smaller than this critical value, no drag force between the two solid phases is assumed.

E. *Species Conservations and Solute Partitioning at the Solid/Liquid Interface*

The volume-averaged concentration c_l in the liquid, c_e in the equiaxed, and c_c in the columnar phase are obtained by solving the species concentration equations:

$$\frac{\partial}{\partial t}(f_l\rho_l c_l) + \nabla\cdot(f_l\rho_l\mathbf{u}_l c_l) = \nabla\cdot(f_l\rho_l D_l\nabla c_l) + C_{cl} + C_{el} + C_l^s \qquad [17]$$

$$\frac{\partial}{\partial t}(f_e\rho_e c_e) + \nabla\cdot(f_e\rho_e\mathbf{u}_e c_e) = \nabla\cdot(f_e\rho_e D_e\nabla c_e) + C_{le} + C_{ce} + C_e^s \qquad [18]$$

Table I. Definition of Momentum Exchange Terms

Due to Phase Transition		Drag Force
$\mathbf{U}_{le} = \mathbf{U}_{le}^p + \mathbf{U}_{le}^d$	$\mathbf{U}_{le}^p = \mathbf{u}^*\cdot\mathrm{M}_{le}$	$\mathbf{U}_{le}^d = K_{le}\cdot(\mathbf{u}_l - \mathbf{u}_e)$
$\mathbf{U}_{el} = -\mathbf{U}_{le}$	$\mathbf{u}^* = \begin{cases}\mathbf{u}_l & (\textit{solidification})\\ \mathbf{u}_e & (\textit{remelting})\end{cases}$	the drag force coefficient K_{le} refers to Ref. 7
$\mathbf{U}_{lc} = \mathbf{U}_{lc}^p + \mathbf{U}_{lc}^d$	$\mathbf{U}_{lc}^p = \mathbf{u}^*\cdot M_{lc}$	$\mathbf{U}_{lc}^d = K_{lc}\cdot(\mathbf{u}_l - \mathbf{u}_c)$
$\mathbf{U}_{cl} = -\mathbf{U}_{lc}$	$\mathbf{u}^* = \begin{cases}\mathbf{u}_l & (\textit{solidification})\\ \mathbf{u}_c & (\textit{remelting})\end{cases}$	the drag force coefficient refers to Ref. 13 $K_{lc} = -f_l^2\ \frac{\mu_l}{K}$ with $K = 6\times10^{-4}\lambda_l^2\frac{f_l^3}{(1-f_l)^2}$ as permeability
$\mathbf{U}_{ce} = \mathbf{U}_{ce}^p + \mathbf{U}_{ce}^d$	$\mathbf{U}_{ce}^p = \mathbf{u}^*\cdot M_{ce}$	$\mathbf{U}_{ce}^d = K_{ce}\cdot(\mathbf{u}_c - \mathbf{u}_e)$
$\mathbf{U}_{ec} = -\mathbf{U}_{ce}$	$\mathbf{u}^* = \mathbf{u}_c\ (\textit{segmentation})$	$K_{ce} = \begin{cases}\infty & (f_c \ge f_c^{\mathrm{free}})\\ 0 & (f_c < f_c^{\mathrm{free}})\end{cases}$ $f_c^{\mathrm{free}} = 0.2$

$$\frac{\partial}{\partial t}(f_c \rho_c c_c) + \nabla \cdot (f_c \rho_c \mathbf{u}_c c_c) = \nabla \cdot (f_c \rho_c D_c \nabla c_c) + C_{lc} + C_{ec} + C_c^s \qquad [19]$$

Solute exchange terms acting during solidification are defined in Table II. No additional sources are considered; hence, we have set $C_l^s = C_e^s = C_c^s = 0$.

F. *Enthalpy Conservation*

We solve the enthalpy conservation equation for each phase:

$$\frac{\partial}{\partial t}(f_l \rho_l h_l) + \nabla \cdot (f_l \rho_l \mathbf{u}_l h_l) = \nabla \cdot (f_l k_l \nabla \cdot T_l) + Q_{cl} + Q_{el} + Q_l^s \qquad [20]$$

$$\frac{\partial}{\partial t}(f_e \rho_e h_e) + \nabla \cdot (f_e \rho_e \mathbf{u}_e h_e) = \nabla \cdot (f_e k_e \nabla \cdot T_e) + Q_{le} + Q_{ce} + Q_e^s \qquad [21]$$

$$\frac{\partial}{\partial t}(f_c \rho_c h_c) + \nabla \cdot (f_c \rho_c \mathbf{u}_c h_c) = \nabla \cdot (f_c k_c \nabla \cdot T_c) + Q_{lc} + Q_{ec} + Q_c^s \qquad [22]$$

where the enthalpies are defined *via* $h_l = \int_{T_{\text{ref}}}^{T_l} c_{p_{(l)}} dT + h_l^{\text{ref}}$ and $h_e = h_c = \int_{T_{\text{ref}}}^{T_e} c_{p_{(s)}} dT + h_e^{\text{ref}}$ with the specific heat of the liquid $c_{p(l)}$ and the solid phase $c_{p(s)}$. The terms T_{ref} and h_e^{ref} are defined so that the enthalpy difference between the liquid and any solid, $(h_l - h_e)$ and $(h_l - h_c)$, is equal to the latent heat of fusion. The release of latent heat and the enthalpy exchange between the phases are treated as defined in Table III. Further details can be found in previous publications by the authors.[7,8] Again, no additional sources are considered, and thus we have set $Q_l^s = Q_e^s = Q_c^s = 0$. By solving the preceding conservation equations, Eqs. [20] through [22], three different temperatures T_l, T_e, and T_c were obtained. In order to balance the temperatures between the three phases ($T_l \approx T_e \approx T_c$), a quite large volume heat exchange coefficient of $H^* = 10^8$ W/m^3/K is used.

Table II. Definition of Species Exchange Terms

	Solute Partitioning Due to Phase Transition	Diffusive Species Exchange at Interface
$C_{le} = C_{le}^p + C_{le}^d$	$C_{le}^p = c^* \cdot M_{le}$	
$C_{el} = -C_{le}$	$c^* = \begin{cases} k \cdot c_l^* & (\textit{solidification}) \\ c_e & (\textit{remelting}) \end{cases}$	$C_{le}^d = 0$
$C_{lc} = C_{lc}^p + C_{lc}^d$	$C_{lc}^p = c^* \cdot M_{lc}$	
$C_{cl} = -C_{lc}$	$c^* = \begin{cases} k \cdot c_l^* & (\textit{solidification}) \\ c_c & (\textit{remelting}) \end{cases}$	$C_{lc}^d = 0$
$C_{ce} = C_{ce}^p + C_{ce}^d$	$C_{ce}^p = c^* \cdot M_{ce}$	
$C_{ec} = -C_{ce}$	$c^* = c_c \ (\textit{segmentation})$	$C_{ce}^d = 0$

G. *Auxiliary Quantities*

In order to study the macrosegregation quantitatively, a mixture concentration, c_{mix}, is defined according to

$$c_{\text{mix}} = \frac{c_l \cdot \rho_l \cdot f_l + c_e \cdot \rho_e \cdot f_e + c_c \cdot \rho_c \cdot f_c}{\rho_l \cdot f_l + \rho_e \cdot f_e + \rho_c \cdot f_c} \qquad [23]$$

The volume averaging approach relates the volume fraction of the spherical equiaxed grains f_e to the grain number density n by

$$f_e = n \cdot \frac{4\pi}{3} (d_e/2)^3 \qquad [24]$$

This geometrical relation is used to determine the volume-averaged grain diameter d_e. The term f_e is known from the corresponding mass conservation equation (Eq. [4]), and n from the corresponding conservation equation for the grain number density (Eq. [1]).

For the columnar trunks, the corresponding volume fraction f_c can be related to the average cross-sectional area of a single trunk, $\pi \cdot (d_c/2)^2$, over the maximal available area for a hexagonal* dendrite area

$$f_c = \frac{3}{4} \cdot \frac{d_c^2}{\lambda_1^2} \qquad [25]$$

This geometrical relation is used to determine the volume-averaged dendrite trunk diameter, d_c. Again, f_c is known from the corresponding mass conservation equation

Table III. Definition of Enthalpy Exchange Terms

	Latent Heat of Solidification & Melting	Volume Heat Exchange
$Q_{le} = Q_{le}^p + Q_{le}^d$	$Q_{le}^p = h^* \cdot M_{le}$	$Q_{le}^d = H^* \cdot (T_l - T_e)$
$Q_{el} = -Q_{le}$	$h^* = \begin{cases} h_l & (\textit{solidification}) \\ h_e & (\textit{remelting}) \end{cases}$	H^* *infinitive* (10^8 W/m^3/K)
$Q_{lc} = Q_{lc}^p + Q_{lc}^d$	$Q_{lc}^p = h^* \cdot M_{lc}$	$Q_{lc}^d = H^* \cdot (T_l - T_c)$
$Q_{cl} = -Q_{lc}$	$h^* = \begin{cases} h_l & (\textit{solidification}) \\ h_c & (\textit{remelting}) \end{cases}$	H^* *infinitive* (10^8 W/m^3/K)
$Q_{ce} = Q_{ce}^p + Q_{ce}^d$		$Q_{ce}^d = H^* \cdot (T_c - T_e)$
$Q_{ec} = -Q_{ce}$	$Q_{ce}^p \equiv 0.0$	H^* *infinitive* (10^8 W/m^3/K)

---

*For a cubic area, the prefactor in Eq. [25] would be $\pi/4$ instead of 3/4.

(Eq. [5]), and λ_1 is given. For the results presented in Section IV, we have used $\lambda_1 = 1$ mm.[13,14,15]

H. *Columnar Tip Front Tracking and Tip Front Stopping Mechanism*

Columnar tip front tracking is based on the assumption that columnar dendrite trunks grow from the wall into the bulk melt, depending on the tip growth speed. However, no growth-preferred crystalline orientation is considered. The columnar tip tracking procedure, which is described in the following paragraphs, can be used for any arbitrary unstructured grid. (1) Each control volume is indexed with a columnar status marker, i_c, which indicates whether the control volume contains the columnar tip front ($i_c = 1$), columnar dendrite trunks ($i_c = 2$), or no trunks or tips ($i_c = 0$). All control volumes are initialized with $i_c = 0$, except the boundary (wall) elements, which are marked with $i_c = 1$, (2) For each control volume, a reference length l_{ref} is assigned by seeing the control volume as an equivalence sphere with a radius of $l_{\text{ref}}/2$. In 3-D cases, the volume of the sphere must be equal to that of the corresponding control volume: $4\pi/3 \cdot (l_{ref}/2)^3 = \Delta V$, (3) The columnar front is assumed to grow parallel to the local heat flow direction with a growth velocity v_{tip}, which is determined using the LGT model.[11,12] The actual position of the front is tracked by the integral $l = \int_t v_{\text{tip}} dt$, starting as soon as the front enters the control volume, (4) For $l > l_{\text{ref}}$, the columnar tip front has grown above the equivalence sphere. In this case, all neighboring control volumes, which are still empty ($i_c = 0$), will be reached by the front. Thus, the columnar status markers of these volumes are set to $i_c = 1$, whereas the marker of the volume under consideration is set to $i_c = 2$. Here, the term ''neighbors'' is used to describe control volumes that have at least one single point of contact with the considered volume, (5) A net mass transfer from the liquid to the columnar phase is only taken into consideration for those control volumes where $i_c \neq 1$, and (6) In order to model the stopping mechanism described by Hunt,[1] the tip growth velocity is set to zero, $v_{\text{tip}} \equiv 0$, as soon as the local equiaxed volume fraction, f_e, increases above the critical threshold of $f_{e,\text{CET}} = 0.49$. This stopping criterion defines what is known in literature as hard blocking. It is obvious that in the current study, the hard blocking criterion divides regions that consist of 100 pct equiaxed grains from regions that reveal at least a columnar fraction. Further discussion on this point is given in Section VI. The so-called soft blocking mechanism for establishing the CET proposed by Martorano *et al.*[5] is automatically included, as v_{tip} vanishes when the local constitutional undercooling disappears (point 3).

I. *Numerical Implementation*

The conservation equations are numerically solved using the control-volume based finite difference CFD software FLUENT,* version 6.2. All phases share a single pressure field, p. The pressure correction equation is obtained from the sum of the normalized mass continuity equations using a so-called phase coupled SIMPLE (PC-SIMPLE) algorithm.[10] The velocities are solved coupled by phases, but in segregated fashion. For each time-step, up to 60 iterations are necessary to decrease the normalized residual of c_l, c_e, c_c, f_e, f_c, $\mathbf{u}_l$, $\mathbf{u}_e$, p, and n to a value below the convergence limit of 10^{-4}, and h_l, h_e, and h_c below that of 10^{-7}. On each iteration, the auxiliary quantities d_e, d_c, and μ_e are updated first. Then, based on the last iteration, the exchange terms U_{le}, U_{lc}, C_{le}, C_{lc}, Q_{le}, and Q_{lc} and the source terms N_e, M_{le}, and M_{lc} are calculated. Finally, the 14** conservation equations for the corresponding momenta, masses, enthalpies, and species are solved simultaneously, which means they are coupled by the amount of the different phases and the exchange and source terms.

The FLUENT formulation is fully implicit. There is no stability criterion that has to be met. However, due to the complexity of the present problem, the time-step Δt should not be too large, to ensure a high enough accuracy. The optimal time-step must be determined empirically by test simulations. For the results presented in Section IV, a time-step of $\Delta t = 10^{-4}$ s was used to start the simulation. In a later stage, it was adjusted to $\Delta t = 10^{-3}$ s. Further discussion about calculation accuracy and the effect of mesh quality (size) upon it can be found in previous publications.[7,8]

III. DEFINITION OF THE BENCHMARK CONSIDERED

The solidification of a binary steel (Fe-0.34 wt pct C) ingot casting with a relatively small size (diameter: 66 mm, height: 170 mm) is simulated (Figure 1). For the same ingot, both 2-D axis symmetrical and 3-D calculations were made. In the case of 2-D axis symmetry, only half of the domain is considered. The grid used consisted of 690 elements, with a mean size of about 8 mm^2. In the case of 3-D geometry, the entire ingot is divided into 41,607 hexahedral volume elements with grid size of 10.5 mm^3. The 2-D simulations were done on a PC cluster (Pentium IV, initat Informationtechnologie GmbH, Vienna, Austria), but only one single CPU node was used. One single 2-D simulation took about 20 hours. The 3-D calculations were carried out on a shared memory machine (SGI Altix 350, Itanium II, Silicon Graphics GmbH, Grasbrunn, Germany). One single 3-D calculation took about 10 days with 8 CPUs running in parallel. The casting is thought to be filled instantaneously, so we assume the solidification to start at a uniform initial temperature of 1785 K. The mold and surrounding air is assumed to remain at 300 K. A heat-transfer coefficient, $H = 700 \text{ W} \cdot \text{m}^{-2} \cdot \text{K}^{-1}$, between the casting and mold, and $H = 100 \text{ W} \cdot \text{m}^{-2} \cdot \text{K}^{-1}$, between the casting and air, is used. Other properties and parameters used for the simulation are listed in Table IV.

IV. SIMULATION RESULTS FOR THE BENCHMARK INGOT

For the 2-D axis symmetrical simulations, the results are shown in Figure 2 through 5, on the whole by mirroring. All

---

*FLUENT is a trademark of Fluent Inc., Lebanon, NH.

**There are 14 equations in 2-D (we count two equations for the momentum of each moving phase), but there are 17 in 3-D.

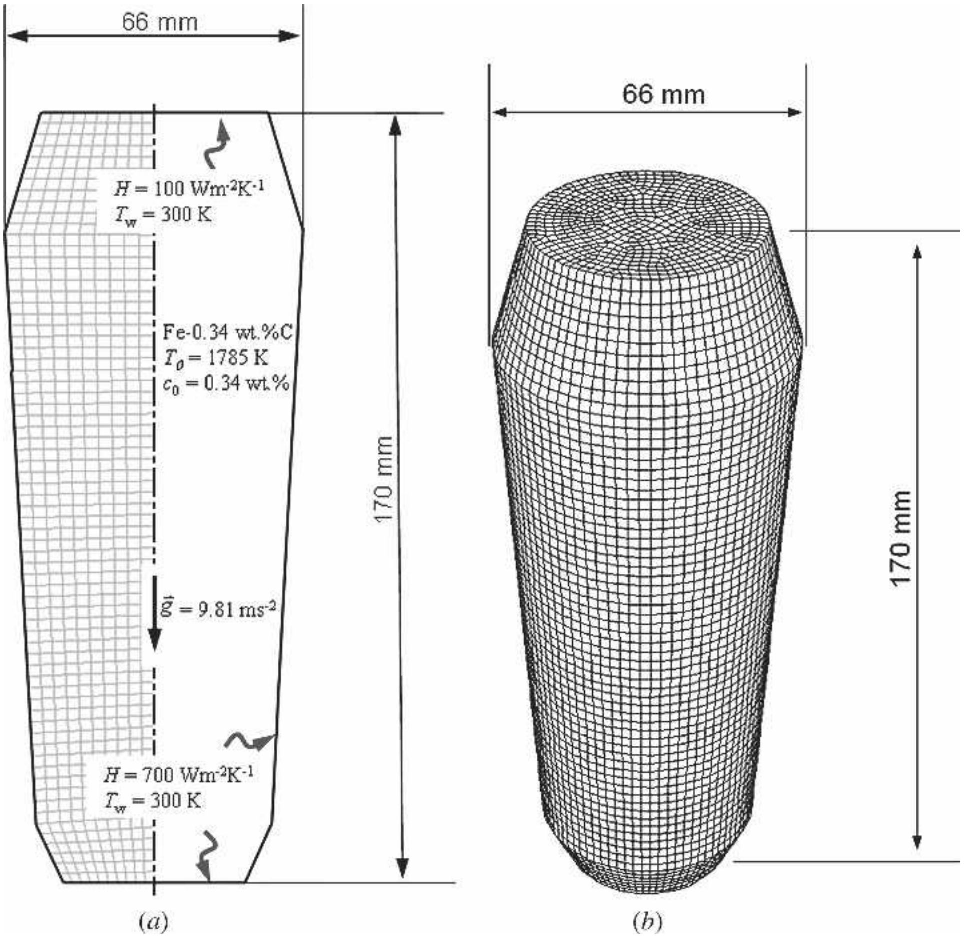

Fig. 1—Schematic of the simulated steel ingot benchmark. (*a*) In the case of 2-D axis symmetrical calculations, only half of the geometry is enmeshed, while (*b*) in the case of 3-D calculations, the entire ingot is enmeshed.

scalar quantities are shown in gray scales, with dark representing the maximum and light representing the minimum value, except for the temperature, which is shown with black as the lowest and bright as the highest temperature. The vectors, $\mathbf{u}_l$ and $\mathbf{u}_e$, are linearly scaled from zero to the maximum velocity.

A. *Solidification Sequences*

Figure 2 shows the solidification sequence of the ingot casting, as predicted from a 2-D axis symmetrical simulation. The overall solidification sequence is dominated by heat transfer. The start of cooling immediately establishes a positive temperature gradient at the outer surface of the casting. At $t = 5$ seconds, the melt in contact with the mold wall has already cooled below liquidus (1782.3 K). Both columnar growth and nucleation and growth of equiaxed grains occur. By definition, the columnar dendrite trunks stick to the mold wall. In contrast to that, the equiaxed grains start to sink along the mold wall. The sinking grains induce melt convection and two symmetrical vortices form. In addition to the grain-sedimentation-induced melt convection, thermal and solute buoyancy also drives melt convection. The melt near the wall has a lower temperature and is thus heavier than the bulk melt ($\beta_T > 0$). As a consequence, the thermal buoyancy effect strengthens the grain-sedimentation-induced melt convection. On the other hand, the effect of solute buoyancy is the reverse of thermal buoyancy. The melt near the mold is enriched with solute; thus, it is less dense ($\beta_c > 0$). From the flow pattern shown in Figure 2, it becomes apparent that the joint effect of thermal buoyancy and grain-sedimentation-induced flow governs the overall convection pattern. Of course, the sedimentation of the equiaxed grains influences their distribution. The equiaxed grains sink downward and settle in the bottom region, where their volume fraction soon reaches a quite high level of, *e.g.,* $f_e = 0.39$ at $t = 5$ seconds.

In the course of further cooling, f_c increases at the mold wall, and the columnar tip front moves inward. The equiaxed grains continue to nucleate, grow, and sink, at first mainly ahead of the columnar front, but later also in the bulk melt. Unless captured by the columnar front, they settle and pile up in the lower region of the ingot. At $t = 20$ seconds, f_c near the wall reaches about 97 pct, and f_e in the lower part of the ingot about 78 pct. However, there is also an increasing amount of equiaxed grains captured by the columnar front due to the corresponding condition defined in Section II–D.

At $t = 60$ seconds, the two columnar tip fronts from both sides have met in the middle of the casting. This leads to the formation of two closed columnar tip front lines: one in the upper region where the temperature is still quite high

Table IV. Properties and Parameters Used for the Simulations

$c_{p(l)} = c_{p(s)} = 808.25\ \mathrm{J \cdot kg^{-1} \cdot K^{-1}}$	$k = 0.2894$
$D_l = 2 \times 10^{-8}\ \mathrm{m^2 \cdot s^{-1}}$	$m = -84.53$ K/wt pct
$D_e = D_c = 5.6 \times 10^{-10}\ \mathrm{m^2 \cdot s^{-1}}$	$T_f = 1811$ K
$\Delta h_f = h_l^{\mathrm{ref}} - h_e^{\mathrm{ref}} = 256{,}476\ \mathrm{J \cdot kg^{-1}}$	$\Gamma = 2.9 \times 10^{-7}\ \mathrm{m \cdot K}$
$k_l = k_e = k_c = 33.94\ \mathrm{W \cdot m^{-1} \cdot K^{-1}}$	$\lambda_1 = 1$ mm
$\beta_T = 0.002\ \mathrm{K^{-1}}$	
$\beta_c = 1.1$	
$\rho_l = \rho_e = \rho_c = 7027\ \mathrm{kg \cdot m^{-3}}$	
$\Delta\rho = 294\ \mathrm{kg \cdot m^{-3}}$	
Process Parameters	Others
$n_{\max} = 5 \times 10^9\ \mathrm{m^{-3}}$	$\Delta V \approx 6\ \mathrm{mm^2}$
$\Delta T_N = 5$ K	$\Delta t = 0.001$ s
$\Delta T_\sigma = 2$K	$H^* = 10^{-8}\ \mathrm{W \cdot m^{-3} \cdot K^{-1}}$
Further parameters, see Fig. 1	$f_e^c = 0.637$
	$f_c^{\mathrm{free}} = 0.2$

and the solid fraction is low, and the second in the lower part of the casting, where the temperature is low and the solidification is nearly completed, mainly with equiaxed grains ($f_e \geq 0.99$).

At $t = 90$ seconds, the solidification of the entire casting is almost finished. The columnar tip front in the upper part of the casting has disappeared; it met in the middle. However, in the lower part of the casting, the columnar tip front has ceased to propagate further. This indicates the occurrence of a CET. Within the columnar tip front line, only equiaxed grains exist, while outside of it, both columnar and equiaxed phases coexist.

Figure 3 gives an example of a number of solidification variables (at $t = 20$ seconds) in more detail. The concentration field in liquid phase, c_l, is gradually enriched in the solidifying regions (mushy zone). Although in the casting center c_l still remains close to the initial concentration of 0.34 wt pct C, the melt near the mold wall has already been enriched to 3.7 wt pct C. As explained in Section II–C, the parameter $(c_l^* - c_l)$ is considered to be the driving force for mass transfer (M_{lc}, M_{le}), whereby the equilibrium liquidus concentration c_l^* is directly related to the local temperature $(T = T_f + m \cdot c_l^*)$. The larger the value of $(c_l^* - c_l)$, the larger the net mass transfer rates M_{lc} and M_{le}. The value of M_{lc} is by definition equal to 0 ahead of the tip front. The phase transition from the liquid to the columnar solid occurs only behind the tip front. Of course, the phase transition from the liquid to the equiaxed solid M_{le} occurs independent of the position of the columnar tip front. In addition to the driving force $(c_l^* - c_l)$ a grain number density, n, other than zero is necessary to drive the solidification of equiaxed grains. The value of n is obtained from Eq. [1], either by nucleation or grain transport.

As the net mass-transfer rate is also proportional to the available solid/liquid interface surface area, M_{le} is higher in the bottom regions where grains have already settled and thus a large solid/liquid interface surface area per volume is present. This is similar to the columnar phase at the upper parts of the ingot. There, the relatively high volume fraction leads to a large solid/liquid interface surface area per volume, and this, in turn, leads to a higher net mass transfer, M_{lc}.

It seems surprising to find that the maximum of $c_l^* - c_l$ occurs in the lower corner regions, where solidification is about to end ($f_e + f_c \geq 0.99$). In the case of no grain sedimentation, one would expect $c_l^* - c_l$ to vanish for f_l approaching 0, because the concentration of the residual melt c_l would be enriched dramatically at the end of solidification (Section V–B). With the high settling rate of the equiaxed phase in the corner regions, however, the enrichment of c_l is not as strong. The accumulation of solid phase ($f_c + f_e$) in these regions is due to two facts: the local solidification, which causes the enrichment of c_l, and the settling grains, which do not induce any enrichment of c_l. On the contrary, the settlement of equiaxed grains forces the residual segregated melt to leave these regions. Despite the maximum value of the $c_l^* - c_l$ in the corners, the net mass-transfer rates (M_{lc} and M_{le}) are almost negligible. The reason for this is clear: the corner regions have already been completely solidified ($f_e + f_c \geq 0.99$), and therefore the Avrami factor f_l overwhelms the other factors.

B. *Macrosegregation*

The macrosegregations are shown in Figure 4(b). In order to understand the macrosegregation formation mechanisms, the phase distribution fields f_e and f_c are shown in Figures 4(a) and (c), in three different sections (bottom, middle, and top), corresponding to three different moments (t = 20, 40, and 70 seconds) in time. As already mentioned previously, the initial concentration of the ingot is 0.34 wt pct C. A cone-shaped, negative segregation is predicted in the lower part of the ingot, where high sedimentation rates occur. This negative segregated zone is formed gradually with the solidification process. As the settling grains reveal a lower carbon concentration compared with the melt ($k < 1$), it is obvious that the sedimentation of equiaxed grains leads to negative segregations. The solute-poor equiaxed grains pile up at the bottom of the ingot, and the solute-rich residual melt rises. The distribution of a low mixture concentration c_{mix} is similar to the CET profile.

The positive segregation zone, which forms at the top part of the ingot, is mainly due to melt convection. As mentioned previously, the solute-rich melt rises as the equiaxed grains sink. The solute redistribution in the melt is strongly dependent on the melt convection pattern. As shown in Figure 2, two symmetrical melt vortices occur in the ingot. In the casting center, the flow current transports solute-rich melt from the bottom region toward the top. As the melt hits the casting top, it diverges into two side streams. This causes a left-hand and a right-hand side region enriched with solute elements. Obviously, the positive segregated zones are not stationary during solidification; they move with the flow current until the entire casting has solidified and the melt flow has disappeared.

C. *Grain Size Distribution*

With the given nucleation parameters $n_{\max} = 5 \times 10^9$ $\mathrm{m^{-3}}$, $\Delta T_N = 5$ K, and $\Delta T_\sigma = 2$ K, and a primary dendrite spacing of $\lambda_1 = 1000\ \mu$m, the average equiaxed grain size d_e and the average dendrite trunk diameter d_c are predicted, as shown in Figure 5. The absolute values of d_e and d_c depend on the aforementioned modeling parameters, but the predicted size distribution pattern of Figure 5 reflects the special characteristic of the mixed columnar-equiaxed

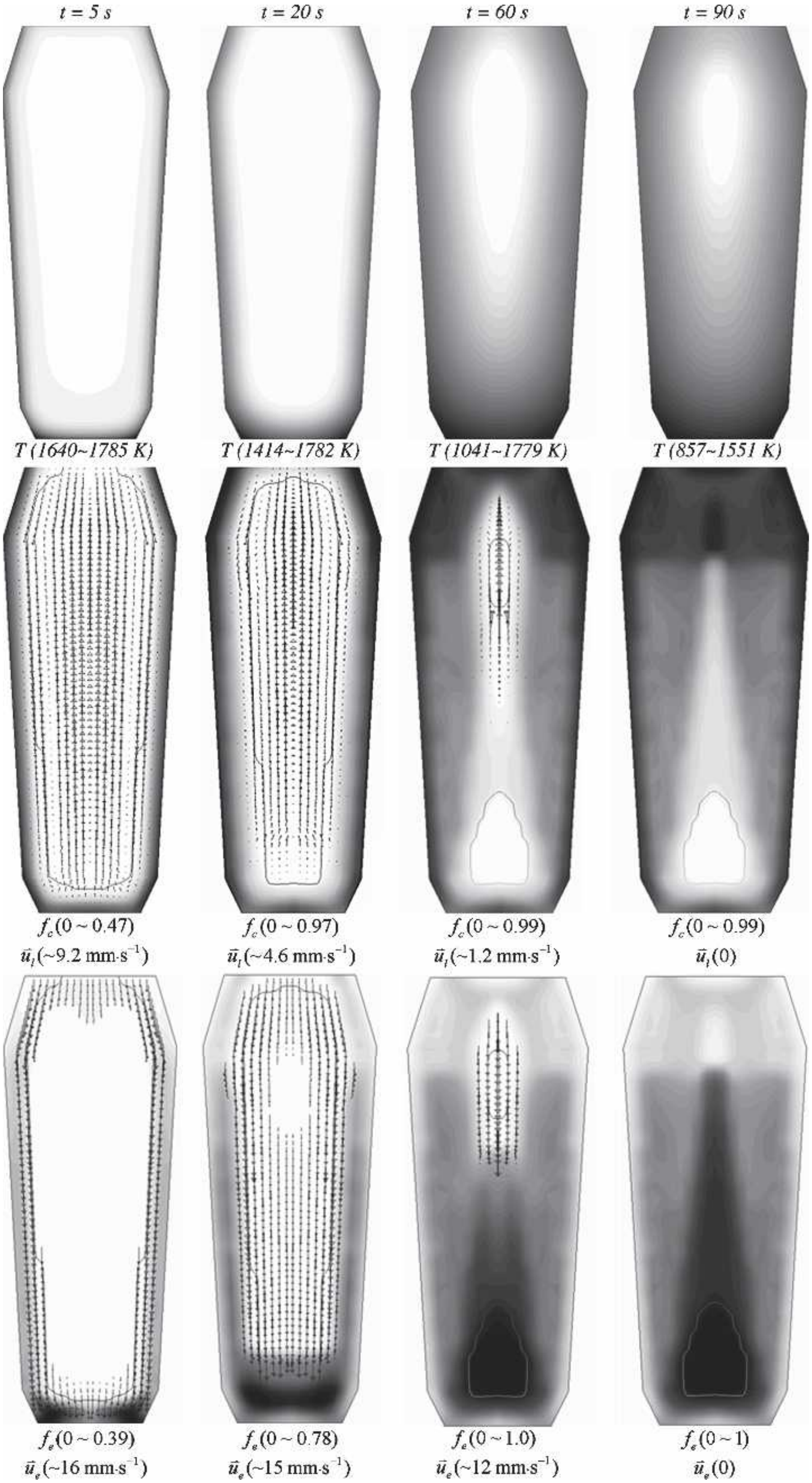

Fig. 2—Solidification sequences for the 2-D axis symmetrical benchmark ingot. All quantities are shown with 60 grayscale levels with maximum and minimum values given. The arrows of both velocities are linearly scaled from zero to the maximum value. The columnar tip front (solid line) is overlaid by the quantities f_c and f_e.

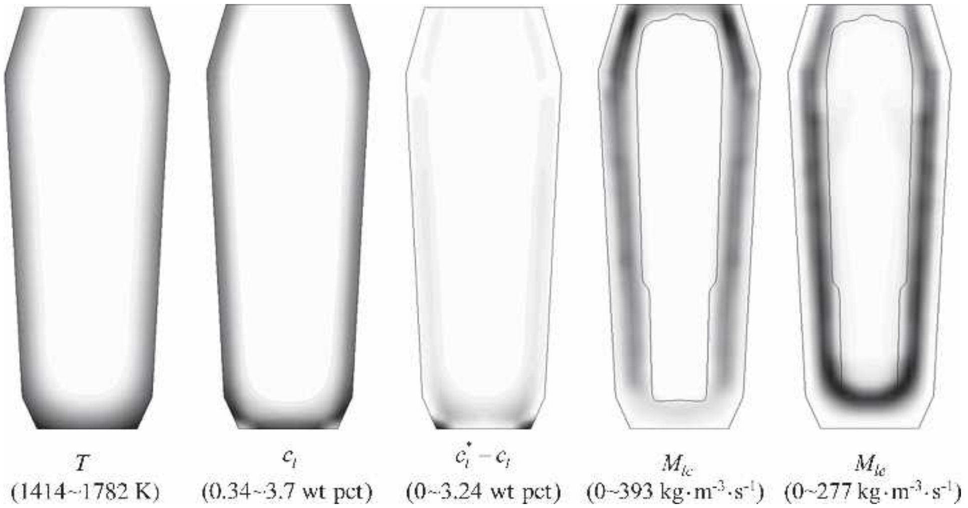

Fig. 3—Temperature *T*, average liquid concentration c_l, and the difference relative to the equilibrium concentration ($c_l^* - c_l$), as well as net mass-transfer rates (M_{lc}, M_{le}), at $t = 20$ seconds for the 2-D axis symmetrical benchmark ingot. All quantities are shown with 60 grayscale levels with the maximum and the minimum values given. The columnar tip envelope is overlaid by the quantities M_{lc} and M_{le}.

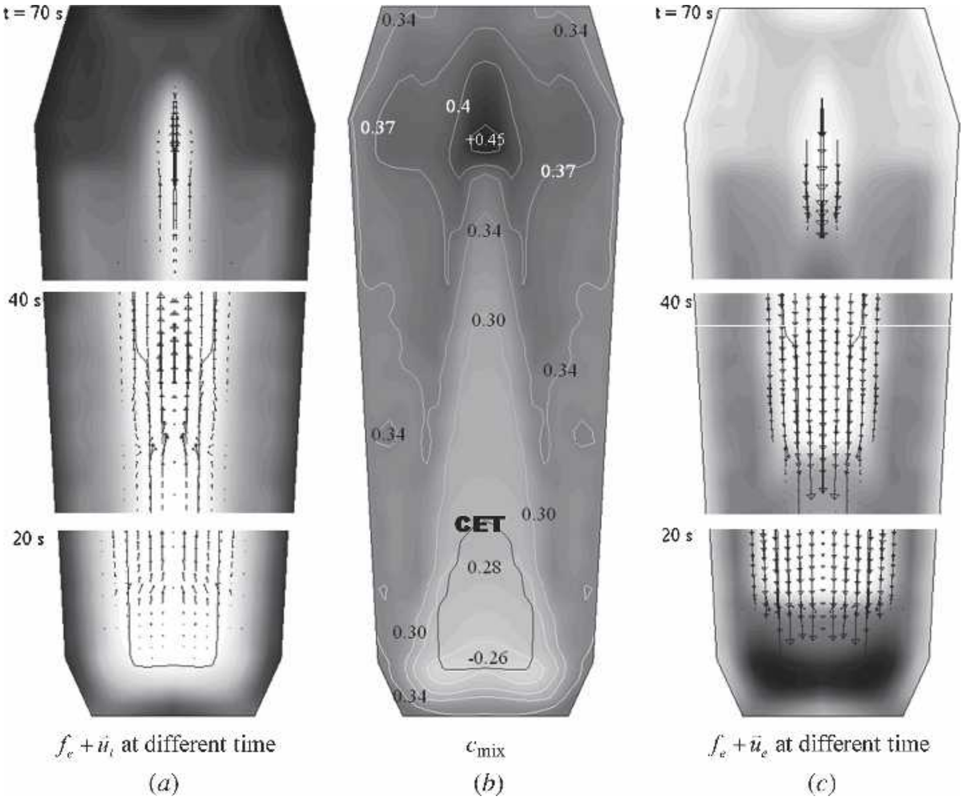

Fig. 4—(*a*) through (*c*) Predicted macrosegregations and their formation mechanisms for the 2-D axis symmetrical benchmark ingot with $c_0 = 0.34$ wt pct C. The term c_{mix} is shown with both isolines and gray scales: light for negative segregation and dark for positive. The values accompanying the isolines are in weight percent. The CET is shown by the black line. The quantities f_c, f_e, $\mathbf{u}_l$, and $\mathbf{u}_e$ are scaled in the same way as in Figure 2. Note that (*a*) and (*c*) give corresponding results for $t = 20$ s, 40 s, and 70 s. The c_{mix} results in (*b*) reveal the final compositions of the ingot.

solidification. In the upper part of the ingot, the average dendrite trunk diameter has reached the maximum possible value, λ_1. This is due to the fact that (1) equiaxed crystals are very scarce ($f_e < 1$ pct) and (2) no interdendritic eutectic solidification was modeled in the present simulation.

Contrary to the upper region, a totally equiaxed zone without any columnar dendrites exists in the area enclosed by the CET line. Those equiaxed grains are not affected by the presence of columnar dendrites and could therefore become quite large.

The cone-shaped distribution pattern for both d_e and d_c is similar to the pattern of the phase volume fractions f_c and f_e, as shown in Figure 2. The general tendency is that the higher the corresponding volume fraction, the larger the grains or trunks. In areas with both columnar dendrite

d_c in μm (0~1000)
(a)

d_e in μm (394~1262)
(b)

Fig. 5—Predicted columnar trunk diameters, d_c, and diameters of the equiaxed grains, d_e, for the 2-D axis symmetrical benchmark ingot. The quantities are shown with gray scales from minimum (bright) to maximum (dark), together with isolines. The CET is shown by the black line.

trunks and equiaxed grains, it must be remembered that the model calculates average quantities. Of course, it is not possible to form trunks with $d_c = 800$ μm and a trunk axis distance of $\lambda_1 = 1$ mm and to place an equiaxed grain with $d_e = 700$ μm between them. However, it is indeed possible for $\lambda_1 = 1$ mm to place an equiaxed grain with $d_e = 700$ μm between two trunks with $d_c = 300$ μm from time to time, and nevertheless get an average trunk diameter of $d_c = 800$ μm.

D. *Grain Transport and Its Impact on the CET*

To demonstrate the importance of grain transport and its impact on the CET, a second simulation was carried out, with a small modification. All conditions and parameters were kept the same, but melt convection and grain sedimentation were switched off. So, the momentum equations for the liquid and the equiaxed phases are not solved in this case. Based on the comparison of the two cases shown in Figure 6, the following statements can be made.

With melt convection and grain sedimentation, the upper and lower parts reveal different evolutions of solid: due to grain sedimentation, the solid is depleted in the upper and gathered in the bottom part of the ingot. In contrast, without melt convection and grain transport, the solid fraction isolines are more or less comparable in the upper and lower regions: they are governed purely by heat extraction from the mold wall.

The location where the last melt solidifies is often called the ‘‘hot spot.’’ In the case having melt convection and grain transport, the hot spot moves significantly upward compared to the case not having these.

In the early stages of solidification, the columnar tip fronts of both cases are similar. As the solidification proceeds, grain sedimentation slows the columnar tip front in the bottom region. Obviously, the existence of settling equiaxed grains hinders columnar tip growth. In addition to deceleration due to settling grains, the decrease in the driving force for solidification $(c_l^* - c_l)$, caused by an above-average increase of the liquid concentration $c_l$in the lower region, which, in turn, results from the flow of solute-rich melt from the side of the ingot, also slows the columnar front.

Furthermore, the melt flow leads to the transport of solute-rich melt from the bottom to the top of the ingot. Again, this causes the liquid concentration c_l in the upper region to increase, and thus to decrease the driving force for solidification $(c_l^* - c_l)$. In consequence, the growth velocity of the columnar tip front v_{tip} is also reduced in the upper region.

In the case having no melt convection and grain sedimentation, the movement of the columnar tip front is relatively uniform in both upper and lower regions. Of course, in this case, no macrosegregation is predicted.

E. *Comparison of 3-D and 2-D Results*

Figures 7 and 8 show results from a 3-D simulation. All the conditions applied and parameters used are the same as those for the 2-D axis symmetrical case (Figure 1(a)). By comparing both simulations (Figure 2 and Figure 7), it turns out that the overall convection and grain sedimentation patterns, the solidification sequences, the predicted phase evolutions, and the final macrosegregations are almost identical. Thus, the explanations given for the 2-D results (Sections IV–A through C) apply also to the 3-D simulation.

However, differences are found in the details. For example, at the initial stage of solidification (t = 5 seconds), the maximum velocities $\mathbf{u}_l$ ($\sim$17 mm $\cdot$ s^{-1}) and $\mathbf{u}_e$ ($\sim$24 mm $\cdot$ s^{-1}) in the 3-D simulation are larger than those in 2-D, where $\mathbf{u}_l$ ($\sim$9.2 mm $\cdot$ s^{-1}) and $\mathbf{u}_e$ ($\sim$16 mm $\cdot$ s^{-1}) were the maxima. The solidification rates at the initial stage (t = 5 seconds) are predicted to be higher for the 3-D simulation. The maxima in f_c and in f_e in 3-D are 0.64 and 0.4, respectively, while the maxima in f_c and in f_e in 2-D are 0.47 and 0.39. Differences in details can also be found at a later stage, where both simulations predict a cone-shaped, CET enclosed equiaxed zone in the lower bottom region of the ingot. The 3-D results show that the CET zone is slightly narrower and more elongated than that of the 2-D simulation.

The reason for the aforementioned differences in details is not yet well understood. The most probable explanation could be found in the different grid fineness and grid types used for the 2-D and the 3-D cases. However, the computational cost for the 3-D benchmark (about 10 days) is too large for any systematical investigation. For the 2-D axis symmetrical benchmark, calculations with different mesh sizes (varying from 1 to 16 mm^2) and mesh types (rectangular and triangular) were made. A 2-D simulation of this type took about 1 day on a PC cluster. The results presented in this article use an average mesh size of about 8 mm^2. They are representative. With a finer mesh, the overall solidification sequence and the final macrosegregation pattern remain almost unchanged, but the CPU time increases dramatically.

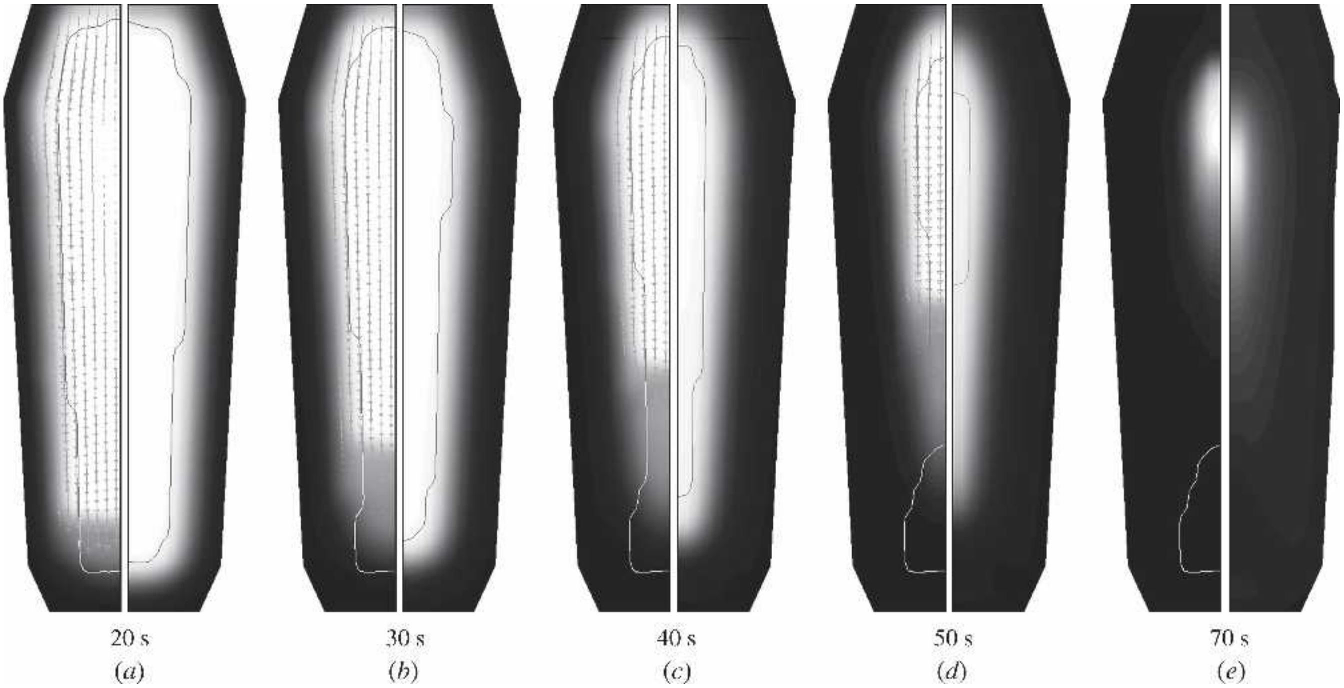

Fig. 6—Comparison of the solidification sequences for the 2-D axis symmetrical benchmark ingot in two cases: the left half is with the melt convection and grain sedimentation, and the right half is without melt convection and grain sedimentation. The grayscale shows the total volume fraction ($f_c + f_e$) with a scaling from 0 (bright) to 1 (dark). In the case of melt convection and grain sedimentation, the velocities of equiaxed grains are shown. Columnar tip front profiles are also indicated with gray or white lines.

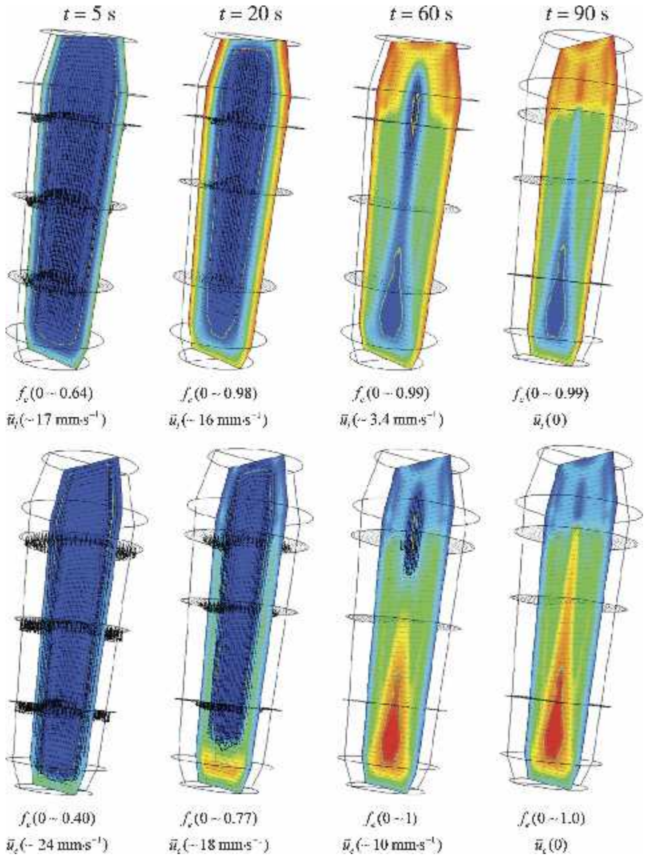

Fig. 7—Predicted 3-D solidification sequences. Both the volume fraction of the columnar phase, f_c, and of the equiaxed phase, f_e, in the central vertical section are shown with a color scale. Their maximum (red) and minimum (blue) values are given. The velocity of the liquid melt, $\mathbf{u}_l$, is shown together with f_c, while the velocity of the equiaxed grains, $\mathbf{u}_e$, is shown with f_e. Additionally, the velocity fields in three horizontal sections are shown. The arrows of the velocities are linearly scaled from zero to the maximum value given. The columnar tip front envelope is shown as a white line.

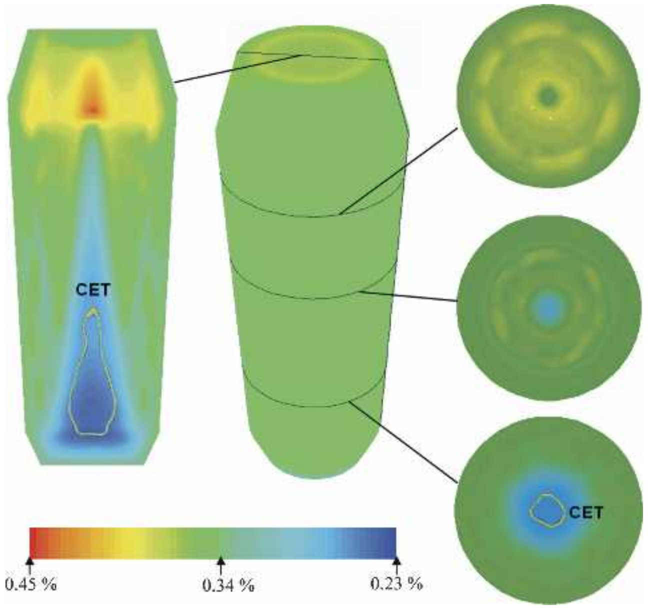

Fig. 8—Predicted final macrosegregation in the 3-D benchmark ingot. The estimated concentration inhomogenities vary from 0.23 to 0.45 wt pct C. The area of 100 pct equiaxed macrostructure is surrounded by the white line.

V. COMPARISON WITH CLASSICAL ANALYTICAL SOLUTIONS

A. *Predicted CET Map*

The first analytical solution (1-D) derived by Hunt[1] stated that the CET should occur when the following condition is met:

$$G < 0.617 \cdot n_{\max}^{1/3} \left(1 - \left(\frac{\Delta T_N'}{\Delta T_{\text{tip}}} \right)^3 \right) \qquad [26]$$

Hunt assumed that all available nucleation sites ($n_{\max}$) operate as soon as the heterogeneous nucleation undercooling, $\Delta T_N'$, is reached. The term ΔT_{tip} represents the columnar dendrite tip undercooling, which depends on the imposed growth velocity *V*, the temperature gradient *G*, and the alloy composition c_0. According to Eq. [26], a CET occurs at a high dendrite tip undercooling ΔT_{tip} (and therefore a high growth velocity *V*) and a low temperature gradient *G*. This statement was widely proven to be true by many experimental and also more detailed theoretical studies, which are summarized and mapped by Kurz and Fischer.[11]

In order to reproduce the CET map with the recent three-phase model, a simple configuration was considered (Figure 9(a)). With adiabatic boundary conditions applied at the top and bottom boundaries, this simple configuration can be thought to represent a 1-D case. The domain is cooled from the left boundary with a constant wall temperature, T_w, and a constant heat-transfer coefficient, H_w, acting between the domain and the wall. A symmetrical plane is defined as the right boundary. Solidification shrinkage and melt flow are not taken into consideration. The assumed material and process parameters are the same as those given in Table IV, except for the ones defined in the figure caption. As an initial condition, a melt with a uniform temperature, T_0, and a uniform concentration, c_0, was assumed.

The solidification process occurring in this simplified configuration is transient. Figure 9(b) shows the phase distributions at $t = 340$ seconds, after the cooling has started. A CET has already occurred at $t = 296$ seconds, $x_{\text{CET}} = 29$ mm away from the wall. Behind the CET, both the columnar and the equiaxed phases coexist, while in front of the CET, only equiaxed grains exist. For the results presented in Figure 9(b), equiaxed grains are always present in the columnar mush. Its volume fraction increases from 20 pct to around 60 pct right at the CET. The reasons for the presence of equiaxed grains in the columnar mush are the chosen nucleation parameters in combination with the growth conditions. Nucleation of equiaxed grains occur right in front of the columnar dendrite tips. Immediately after nucleation, they pass by the columnar dendrite trunks, where they subsequently grow in competition with the columnar dendrite trunks. Note that in the 1-D case presented, the columnar dendrites are stopped by the hard blocking mechanism, that is, f_e exceeds 49 pct.

In order to correlate the CET with *V* and *G*, over 20 different simulations were made by varying the process parameters (initial temperature $T_0 = 1785$ to 1805 K, wall temperature $T_w = 300$ to 500 K, and heat-transfer coefficient $H_w = 100$ to 2000 W $\cdot$ m^{-2} $\cdot$ K^{-1}). Each simulation

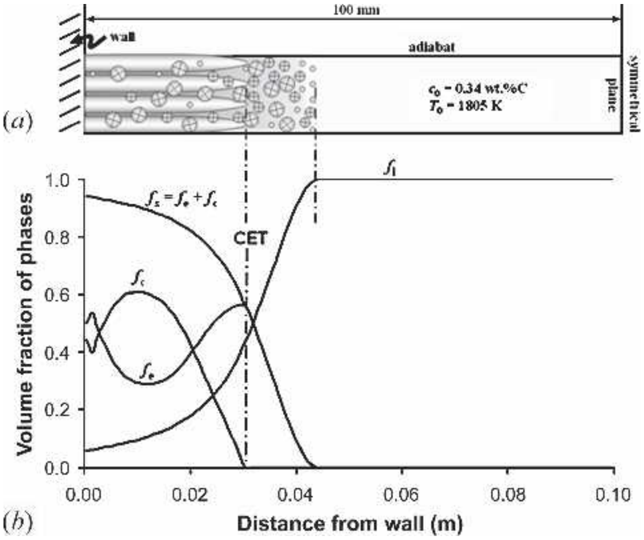

Fig. 9—Phase evolution and CET for an unsteady 1-D directional solidification of a Fe-0.34 wt pct C alloy. (*a*) Schematic sketch of the columnar mush with coexisting equiaxed grains and equiaxed grains ahead of the columnar front. (*b*) Predicted phase distribution at t = 340 s. The process parameters used for this simulation were $T_w = 500$ K, $H_w = 200$ W · m^{-2} · K^{-1}, $n_{\max} = 10^{10}$ m^{-3}, $\Delta T_N = 3$ K, and $\Delta T_\sigma = 1$ K.

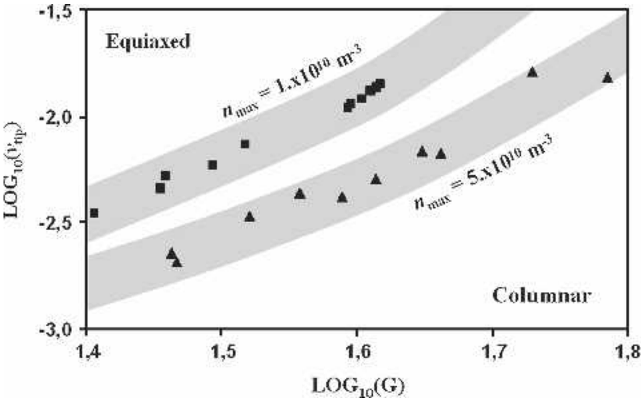

Fig. 10—Predicted CET map for a Fe-0.34 wt pct C alloy gained from simulation, as shown in Figure 9. The columnar tip growth velocity v_{tip} (cm · s^{-1}) at the instant of CET is taken for *V*, and the corresponding temperature gradient at the tip position is taken as *G* (K · cm^{-1}). Heterogeneous nucleation is considered with a three-parameter Gaussian nucleation law, with $\Delta T_N = 3$ K, $\Delta T_c = 1$ K, and $n_{\max}$, as shown in figure.

was run until a CET occurred. The corresponding columnar tip growth velocity v_{tip} was taken for *V*. As the temperature gradient varies during the transient solidification process, *G* at the tip of the trunks was taken at the exact instant of the CET. In Figure 10, the corresponding CET predictions are gathered. Independent of the chosen parameters T_0, T_w, and H_w, all the CET points fall at a log *V*-log *G* plot into a gray band. This gray band divides the plot into two parts: columnar growth (together with equiaxed grains in the columnar mush) in the lower right and equiaxed growth only in the upper left. This result agrees well with former studies.[1,11] With an increasing density of nuclei from $n_{\max} = 1 \times 10^{10}$ m^{-3} to 5×10^{10} m^{-3}, our model predicts a shift of the CET band toward the lower-right corner of the plot. Again, this is in agreement with the prediction of Hunt's model.[1]

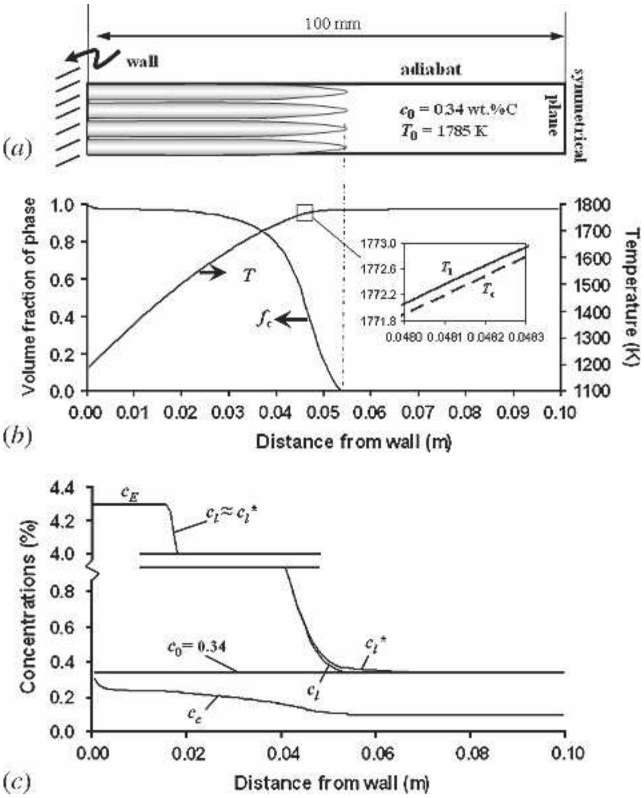

Fig. 11—Solute redistribution in the mushy zone for an unsteady 1-D directional solidification of a Fe-0.34 wt pct C alloy. (*a*) Schematic sketch of the columnar mush. (*b*) Predicted temperature profile and phase distribution at t = 200 s. (*c*) Corresponding concentration profiles. The process parameters used for this simulation were $T_w = 500$ K and $H_w = 700$ W · m^{-2} · K^{-1}.

Note that many experimental and analytical studies on CET are based on an ''imposed'' growth velocity *V* and temperature gradient *G*. In our simplified 1-D configuration, only the process parameters T_0, T_w, and H_w are imposed, whereas *V* and *G* are obtained as modeling results. Thus, a transient case is compared with a quasi-steady-state consideration. However, for the variation range of the process parameters, *V* and *G* are found to fall into a limited range, being relatively narrow compared to previous studies.[1,5,11]

B. *Solute Redistribution during Columnar Solidification*

In order to compare microsegregation predictions made by the present model with classical Gulliver–Scheil results, the solute redistribution in the mushy zone of a 1-D columnar dendrite array is investigated. Figure 11(a) shows a schematic sketch of the configuration. Only two phases are considered: liquid and columnar. The boundary conditions and parameters used are equal to the ones used in Section A, except for those mentioned in the figure caption.

As described in Section II–F, the enthalpy conservation equation is solved for each phase. Therefore, two temperature profiles, T_l and T_c, are obtained. With a large heat exchange coefficient of $H^* = 10^8$ W · m^{-3} · K^{-1} applied between the two phases, the two temperature profiles are almost identical. The maximum temperature difference, t = 200 seconds, after cooling has started, was found to be 0.2 K.

This temperature difference is located in the mushy zone, where a large amount of latent heat is released (Figure 11(b)).

The volume-averaged concentrations at $t = 200$ seconds, after cooling has started, are shown in Figure 11(c). As outlined in Section II, the equilibrium concentration, c_l^*, is calculated according to the local temperature of the melt, T_l. The difference relative to the volume-averaged concentration in the liquid, $(c_l^* - c_l)$ serves as the driving force for solidification. This driving force vanishes gradually with the increase of the solid phase and with the corresponding enrichment of the interdendritic liquid. Figure 11(c) shows that c_l increases from c_0 at the dendrite tips to the eutectic composition, c_E, at the roots of the dendrites. The corresponding $c_l - f_s$ curve is shown in Figure 12(c). It agrees remarkable well with the Gulliver–Scheil curve, at least for $t = 200$ seconds. However, Figure 12 also shows the $c_l - f_s$ curves for (a) $t = 10$ seconds and (b) $t = 50$ seconds. In fact, besides the Gulliver–Scheil curve, three different calculated $c_l - f_s$ curves are presented: (1) without consideration of solidification shrinkage and feeding flow but with a realistic diffusion coefficient, $D_l = 2 \cdot 10^{-8} \cdot \text{m}^2 \cdot \text{s}^{-1}$; (2) same as (1) but with an artificially enlarged diffusion coefficient of $D_l = 10^{-7} \cdot \text{m}^2 \cdot \text{s}^{-1}$; (3) with consideration of solidification shrinkage and feeding flow ($\rho_l = 7027 \text{ kg} \cdot \text{m}^{-3}$ ($\rho_s = 7324 \text{ kg} \cdot \text{m}^{-3}$)), and the artificially enlarged diffusion coefficient from (2). The last case was carried out with a "pressure inlet" condition at the right wall ($T_l^{in} \equiv 1785$ K, $c_l^{in} \equiv 0.34$ wt pct, $p^{in} \equiv 10^5$ Pa), rather then a "symmetrical plane" as the boundary condition. It turns out that the calculated curves are quite close to the Gulliver–Scheil curve for $t = 200$ seconds, *i.e.,* at a low cooling rate. At $t = 10$ seconds, *i.e.,* at an increased cooling rate, the difference between the calculated and the Gulliver–Scheil curves becomes more significant. The Gulliver–Scheil model is based on the assumption of ideal diffusion of solute element in melt, *i.e.,* $c_l^* \equiv c_l$. However, in the present model, a diffusion-controlled growth model is applied by using Eqs. [6] and [9]. The difference, $(c_l^* - c_l)$, governs the diffusion rate, and thus the net mass transfer. For lower cooling rates, more time for diffusion is available to level out $(c_l^* - c_l)$ compared to higher cooling rates. Thus, for low cooling rates, $c_l^* \approx c_l$ is established and the results are closer to those obtained when ideal diffusion is assumed, namely, those of the Gulliver–Scheil approach. Diffusion can also be improved artificially by increasing the diffusion coefficient. Therefore, it is to be expected that the results obtained with a larger D_l will be closer to the Gulliver–Scheil curve. This statement is shown to be true in Figure 12.

During shrinkage-induced feeding flow, segregated melt is transported along the dendrite trunks toward the roots of the dendrites and therefore the $c_l - f_s$ curve is shifted slightly to the upper left side of the Gulliver–Scheil curve. This mechanism will cause macrosegregation to occur, as discussed in detail in Section C.

C. *Feeding-Induced Macrosegregation*

A general expression for the local change of solute redistribution, including consideration of interdendritic flow, was derived by Flemings:[16]

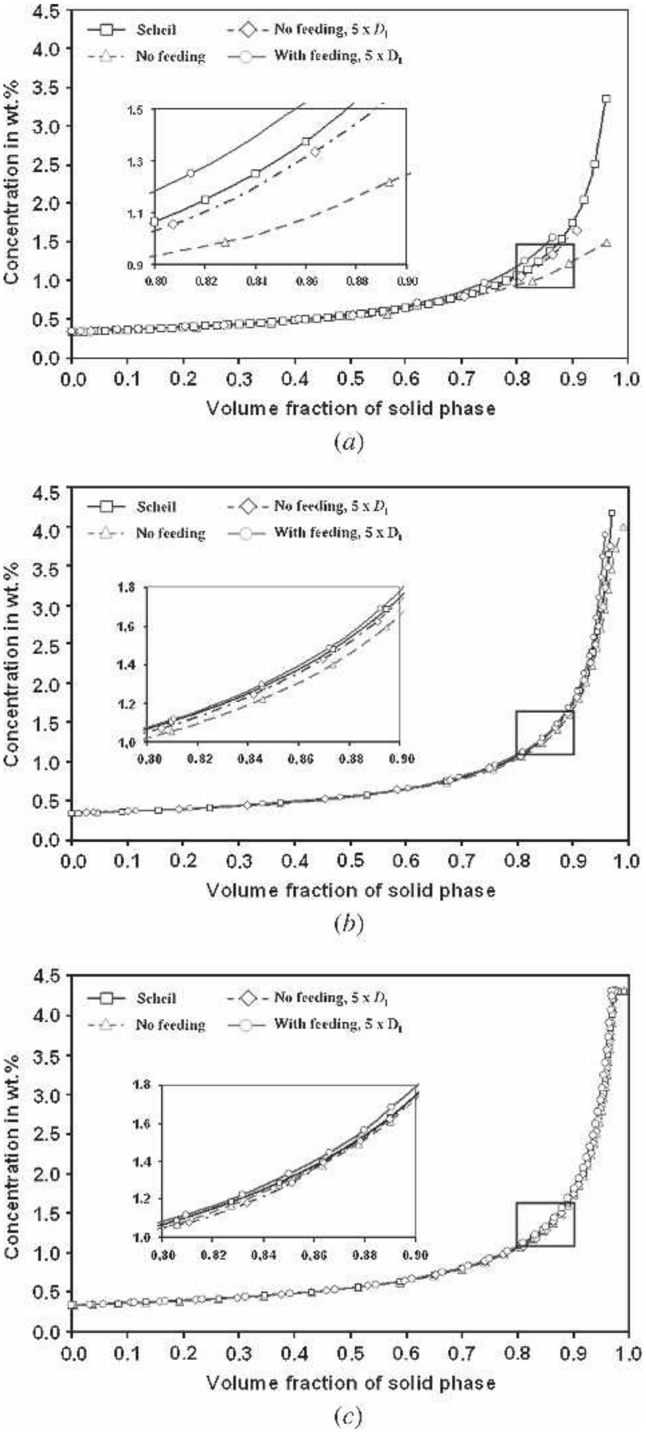

(*a*)

(*b*)

(*c*)

Fig. 12—Plot of the Gulliver–Scheil curve and corresponding $c_l - f_s$ curves at (*a*) $t = 10$ s, (*b*) $t = 50$ s, and (*c*) $t = 200$ s gained from simulations like those shown in Figure 11 for different conditions.

$$\frac{df_l}{dc_l} = -\frac{(1-\beta)}{(1-k)}\left(1 + \frac{\Delta \mathbf{u} \cdot G}{\partial T/\partial t}\right)\frac{f_l}{c_l} \qquad [27]$$

Here, β is the solidification shrinkage, $\beta = (\rho_s - \rho_l)/\rho_s$, $\partial T/\partial t$ is the cooling rate, and $\Delta \mathbf{u}$ is the relative velocity between the melt and the solid. When the solid is stationary, $\Delta \mathbf{u}$ is equal to $\mathbf{u}_l$. Based on Eq. [27], analytical 1-D solutions were obtained[16,17] for limited cases in which only feeding flow and special process conditions are considered. These analytical solutions were proven by Kato *et al.,* experimentally.[18] The feeding-induced macrosegregation was found to be strongly dependent on the applied process conditions.

In the present article, the simple 1-D configuration shown in Figure 11(a) is used to check the model against Flemings' expression. Feeding flow is activated by applying a "pressure inlet" as a boundary condition at the right side of the domain, thus letting hot melt ($T_l^{in} \equiv 1785$ K, $c_l^{in} \equiv 0.34$ wt pct, $p^{in} \equiv 10^5$ Pa) be sucked into the domain to feed solidification shrinkage.

The calculated solidification sequence and the predicted macrosegregations are shown in Figures 13 and 14. Before the columnar dendrite tips approach the end of the domain (*i.e.,* pressure inlet), the positions of (1) the liquidus isotherm, x_{T_L}, (2) the columnar tip front, x_{tip}, and (3) eutectic isotherm, x_{T_E}, can be approximated as linear functions of $\sqrt{t}$ (Figure 13). This kind of solidification sequence represents the typical situation for unidirectional solidification against a cold mold with finite resistance to heat transfer at the mold/metal interface. The slope of the $x_{\text{tip}} - \sqrt{t}$ curve is larger ($m_{\text{tip}} \approx 0.004067$) than the slope of the $x_{T_E} - \sqrt{t}$ curve ($m_E \approx 0.0026$), which means that the thermal gradient in the mushy zone decreases with time, or in other words, the mushy zone extends with time. Note that in the following we refer to the columnar tip front rather than to the liquidus isotherm as Flemings does. In the original work of Flemings, no constitutional undercooling is taken into consideration, and so the columnar tip position was assumed to be at liquidus. The distance from the liquidus isotherm to the columnar tip front turned out to be quite large, but because of the low-temperature gradient in that region, the temperature difference is small. For example, at $t = 200$ seconds, the tip front temperature is predicted to be only $\Delta T_{\text{tip}} = 1.33$ K below liquidus. The solidification sequence shown in Figure 13 is quite similar to the process conditions used by Flemings (curve (2) of Figure 7 in Reference 16). For this case, Flemings predicted the maximum positive segregation (inverse segregation) to occur on the casting surface, an imperceptible positive segregation to occur overall in the casting, and a negative segregation to occur only at end of solidification, when feeding is insufficient. The results gained with our simple 1-D configuration agree with Flemings' analytical results (compare Figure 14 with, for example, curve (2) of Figure 7 in Reference 16). In fact, Figure 14 shows c_{mix} curves for three different moments, so that the evolution of the macrosegregations can be seen. It is interesting to note that the c_{mix} very close to or behind the columnar tip front is always lower than c_0. The reason for this is that the segregated melt from this region is transported into the mush and so replaced by the fresh melt with c_0. However, in the columnar root region, solidification shrinkage is continuously fed by highly segregated melt, and thus, c_{mix} increases, resulting in a positive macrosegregation. As our numerical domain is fed by hot melt, no real end of solidification can be reached. Nevertheless, at a late stage ($t = 700$ seconds), a strong negatively segregated zone is predicted at the end of the casting sample.

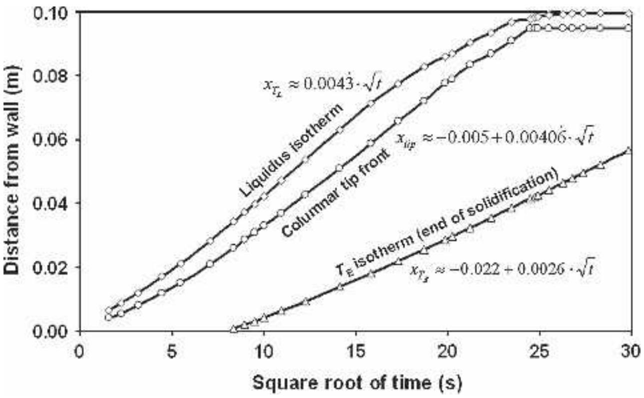

Fig. 13—Numerically calculated liquidus isotherm, columnar tip front, and eutectic isotherm (end of solidification) as a function of the square root of time for $T_0 = 1785$ K, $T_w = 300$ K, and $H = 700 \text{ W} \cdot \text{m}^{-2} \cdot \text{K}^{-1}$.

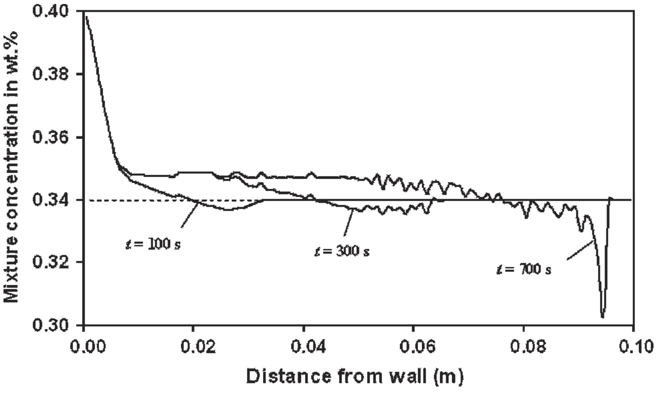

Fig. 14—Predicted macrosegregation formation with consideration of solidification shrinkage induced feeding flow in a 1-D columnar solidifying sample, similar to that shown in Figure 11(a) for $t = 100$ s, 200 s, and 300 s. Note the correspondence to curve (2) of Figure 7 in Reference 16.

VI. DISCUSSION

A. *Potentials of the Three-Phase Model*

With present-day computing resources, only two methods are actually able to model the mixed columnar-equiaxed solidification of castings at an industrial scale, including CET: one is the deterministic model based on the volume averaging approach,[4,5] and the other is the stochastic model, *i.e.,* the cellular automaton technique.[3,19,20] However, the CET models developed so far did not properly account for the effect of melt convection and sedimentation.[3,21] In References 7 and 8, the authors have presented a two-phase deterministic model for equiaxed solidification based on volume averaging, which includes melt convection and grain transport. The recent three-phase model is an extension of this two-phase model, which now also includes the stationary columnar phase for 2-D and 3-D cases. The previous two-phase model for globular equiaxed solidification was compared with experiment and reasonable agreement was obtained.[25] However, the model in recent form, *i.e.,* three-phase including CET, has not been evaluated by direct comparison with experimental data. The reason for this is that, on one hand, reliable materials properties and process parameters are required, and on the other hand, some improvements of the model are necessary (as subsequently discussed). Nevertheless, the results presented for the 2-D/3-D steel ingot benchmark have reproduced the typical experimentally observed solidification phenomena reported often in the literature: (1) The simulated solidification sequence, the sedimentation of the equiaxed grains, the movement of the columnar tip front, and the final macroscopic phase distribution (Figure 2) fit with the widely accepted explanations of experimental findings, as summarized by Campbell:[22] "The fragments (equiaxed grains) fall at a rate somewhere between that of a stone and snow. They are likely to grow as they fall if they travel through the undercooled liquid just ahead of the growing columnar front, possibly by rolling or tumbling down this front. The heap of such grains at the base of the ingot has a characteristic cone shape." One must keep in mind that, in reality, the origin of the equiaxed grains may be due to different mechanisms,[21] *e.g.,* nucleation or fragmentation and detachment of dendrites by remelting or nucleation formed during pouring by contact with the initial chilling of the mold. As stated previously, the recent model condenses all these phenomena into a single "effective" nucleation description, (2) Formation mechanisms for the macrosegregations in binary systems, which solidify with a purely equiaxed structure, were modeled and discussed in detail previously.[7,8,23–25] The macrosegregation formation mechanisms in the presence of both columnar and equiaxed microstructures are much more complicated. A widely accepted opinion about the formation of the cone-shaped negative segregation at the base of the steel ingot is expressed in Campbell's words: "The heap of such fragments (equiaxed grains) at the base of the ingot has a characteristic cone shape. Because it is composed of dendritic fragments, its average composition is that of rather pure iron, having less solute than the average for the ingot. The region is therefore said to have negative segregation." A further contributing factor to the purity of the equiaxed cone region probably arises from the divergence of the flow of residual liquid through this zone at a late stage in solidification, as discussed by Flemings.[26] The simulated negative segregation formation process in the base region of the ingot (Figure 4) seems to have reproduced the experimental phenomenon.

Mechanisms for positive segregations in steel ingots are diverse.[22,27] It is generally agreed that they are caused by the melt convection in the bulk region or through the partially solidified or remelted mushy zone. For example, the upper positive segregation is explained by the melt convection in the bulk region, because the light solute-rich melt rises. We also found this mechanism appearing in our results (Figure 4). The numerical prediction of the large central positive segregation in the upper region coincides with the early experimental results of Nakagawa *et al.*[22,28] The channel segregations, which were often observed in steel ingots, *e.g.*, A segregation and V segregation, are believed to be caused by the channel flows through the mushy zone. The formation of the channel flows is related to the remelting of columnar dendrites. As stated previously (Section II–C), the melting of solid phases is not considered in this work; hence, no A segregation and V segregation are obtained in the simulation results, (3) This article demonstrates the possibility to calculate the macroscopic distribution of columnar and equiaxed phases (Figure 2 and 5). The upper region of the ingot mainly consists of columnar dendrites, whereas a larger amount of equiaxed grains are predicted in the lower region. Within the CET enclosed region, only the equiaxed phase exists, while outside the CET region, both columnar and equiaxed phases coexist. The exact microstructure distribution depends on the process parameters used, *i.e.*, the equiaxed nucleation parameters ΔT_N, $n_{\max}$, ΔT_σ, and the primary columnar space λ_1.

B. *Refinements of the Model and Future Studies*

1. *Physical modeling aspects*

The recent model is based on the assumption of simplified morphologies: equiaxed grains are approximated by spheres and columnar dendrites by cylinders. Both numerical[29,30] and experimental[31] studies have shown that for many alloys, these approximations are rough. Therefore, the results and the predictions of the model could be improved if the real dendritic nature of equiaxed grains and columnar dendrites were taken into account.

Furthermore, a one-dimensional steady-state diffusion-controlled crystal growth model is used to approximate the growth velocity. However, the diffusion field ahead of the liquid-solid interface is, to a certain extent, influenced by melt convection. Thus, the growth kinetics should be modified, for example, by introducing a corresponding Sherwood number in order to account for this effect.[32]

As discussed previously, the assumption of a constant value for the primary dendrite arm spacing, λ_1, is sometimes crude. The numerical model should be modified to consider λ_1 as dependant on process parameters.[11]

For industrial castings, multicomponent alloy systems, detailed mechanical interactions between moving equiaxed and stationary columnar phases, and fragmentation of columnar dendrite trunks or arms are also important facts yet to be included in a more advanced numerical model.

2. *Numerical calculation accuracy*

There are many numerical factors that influence the calculation accuracy: grid size, dimension (2-D and 3-D), grid type (structured and unstructured), time-step, convergent criterion, discretization schemes, differences in the solvers, etc. Most of them can be chosen by referring to the recommendations of the software user manual (in our case, the FLUENT manual[10]), but some parameters must be determined by trial calculations. An often-used method is to repeat the calculation until a numerical-parameter-independent result is reached. A very recent study has shown that complete numerical parameter independence (here, grid independence) seems to be difficult to achieve due to the limiting factor of calculation costs.[33] With present-day computation resources, one has to find a compromise between calculation costs and accuracy. In the present article, we have presented results for a 2-D axis symmetrical and a 3-D simulation. The results have shown the identity of the overall solidification sequence, convection and grain sedimentation patterns, predicted final phase distribution, and macrosegregations. However, the 3-D simulation took more than 10 days on a shared memory workstation, whereas the 2-D axis-symmetrical case only took days on a single node of a PC cluster. Thus, calculations with different mesh sizes and mesh types (rectangular and triangular) were made only for the 2-D axis symmetrical geometry.

If the details, such as the formation of channel segregations (freckle), are to be simulated, a much finer grid (as fine as 0.1 mm, or even smaller) must be used.[33] At present, such a fine grid seems to be impractical for industrial scale castings. A solution to this would be to wait until sufficient computer power is available. On the other hand, the calculation costs can also be reduced by using advanced numerical techniques, such as an unstructured mesh with different mesh sizes in different regions depending on the necessary accuracy. We are currently working on this.

VII. CONCLUSIONS

A three-phase model was developed for mixed columnar-equiaxed solidification. The model accounts directly for the nucleation and growth of the equiaxed globular grains, the columnar growth of dendrite trunks (including the progress of the columnar tip front and CET), and the effect of equiaxed grain sedimentation and melt convection. The 2-D axis symmetrical and 3-D simulations for a binary steel benchmark ingot have demonstrated that many frequently reported experimental phenomena known from steel ingots can be modeled with the model presented here.

1. The simulated solidification sequence, the sedimentation of equiaxed grains, the movement of the columnar tip front, and the final macroscopic phase distribution agree with the classical explanations of ingot solidification. The columnar dendrite trunks grow from the mold wall toward the middle of the ingot. Equiaxed grains nucleate near the mold walls, ahead of the columnar front, and also in the bulk melt. The columnar phase grows affixed to the wall, whereas the equiaxed phase sinks and settles at the bottom of the ingot.
2. The modeling results confirm cone-shaped negative segregations, which are typically found in steel ingots. The main mechanism for this cone-shaped negative segregation is grain sedimentation. The sinking grains pile up in the bottom region. These settling grains are poor in solute element, and hence induce negative segregation. A further contributing factor to this negative segregation arises from the divergence of the flow of the residual liquid through this zone at a late stage in solidification. The model also predicts a positive segregation in the upper region of the ingot. Because the remelting of the solid phase has not been taken into account, no channel segregations are simulated in the current model.
3. The benchmark simulations also show the ability to calculate the microstructure, including the macroscopic phase distribution. It is known from practice that equiaxed grains are found to a large extent in bottom and base regions of steel ingots, whereas in the upper region, more columnar growth morphology is found. However, from our experience, it became obvious that the absolute values for grain sizes or dendrite trunk diameters strongly depend on the process parameters. As far as possible, these parameters should carefully be determined through corresponding experiments.
4. The comparison of a simulation that considers melt convection and grain sedimentation with a second simulation that ignores any motion showed that (1) the effect of the grain sedimentation and melt convection makes the hot spot of the ingot shift upward; (2) for the case with melt convection and sedimentation, a CET is predicted, while for the other case no CET occurs; and (3) as expected, macrosegregations only form with melt convection or grain sedimentation.
5. The model was evaluated by comparing it with classical analytical models based on limited 1-D cases and satisfactory agreements were obtained. Nevertheless, in order to apply the model to industrial castings, improvements in some model details and further parameter studies regarding the calculation accuracy and cost are still necessary.

NOMENCLATURE

c_0 wt pct	initial concentration
c_l, c_e, $c_c$wt pct	species concentration
c^{ref} wt pct	reference concentration
c_l^*, c_s^* wt pct	equilibrium concentration at interface
$C_{le}(= -C_{el})$ kg · m^{-3} · s^{-1}	total species exchange between liquid and equiaxed
$C_{le}^d(= -C_{el}^d)$ kg · m^{-3} · s^{-1}	diffusive species exchange between liquid and equiaxed
$C_{le}^p(= -C_{el}^p)$ kg · m^{-3} · s^{-1}	species exchange due to phase change at *l-e* interface
$C_{lc}(= -C_{cl})$ kg · m^{-3} · s^{-1}	total species exchange between liquid and columnar
$C_{lc}^d(= -C_{cl}^d)$ kg · m^{-3} · s^{-1}	diffusive species exchange between liquid and columnar
$C_{lc}^p(= -C_{cl}^p)$ kg · m^{-3} · s^{-1}	species exchange due to phase change at *l-c* interface
$C_{ce}(= -C_{ec})$ kg · m^{-3} · s^{-1}	total species exchange between equiaxed and columnar
$C_{ce}^d(= -C_{ec}^d)$ kg · m^{-3} · s^{-1}	diffusive species exchange between equiaxed and columnar
$C_{ce}^p(= -C_{ec}^p)$ kg · m^{-3} · s^{-1}	species exchange due to phase change at *c-e* interface
C_l^s, C_e^s, C_c^s kg · m^{-3} · s^{-1}	additional source terms in species equations
C_{mix} L	mix concentration
$c_{p(l)}$, $c_{p(s)}$ J · kg^{-1} · K^{-1}	specific heat
D_l, D_e, D_c m^2 · s^{-1}	diffusion coefficient
d_e m	equiaxed grain diameter
D_c m	columnar trunk diameter
$\mathbf{F}_{Be}$ kg · m^{-2} · s^{-2}	buoyancy force of equiaxed phase
$\mathbf{F}_{Bl}$ kg · m^{-2} · s^{-2}	buoyancy force of columnar phase
F_e^s, F_l^s kg · m^{-2} · s^{-2}	source term in N–S equations

f_l, f_e, f_c L	volume fraction of different phases
$f_s = f_l + f_c$ L	volume fraction of solid phase
f_c^{free} L	critical f_c for free moving equiaxed phase
f_e^c L	equiaxed grain packing limit
$\mathbf{g}$ $\mathrm{m \cdot s^{-2}}$	gravity
$\mathbf{g}'_e, \mathbf{g}'_l$ $\mathrm{m \cdot s^{-2}}$	reduced gravity
G $\mathrm{K \cdot m^{-1}}$	temperature gradient
H $\mathrm{W \cdot m^{-2} \cdot K^{-1}}$	heat-transfer coefficient
H^* $\mathrm{W \cdot m^{-3} \cdot K^{-1}}$	volume heat-transfer coefficient between phases
h_l, h_e, h_c $\mathrm{J \cdot kg^{-1}}$	enthalpy
$h_l^{\mathrm{ref}}, h_e^{\mathrm{ref}}, h_c^{\mathrm{ref}}$ $\mathrm{J \cdot kg^{-1}}$	reference enthalpy
Δh_f $\mathrm{J \cdot kg^{-1}}$	latent heat (heat of fusion)
i_c L	columnar status marker
K $\mathrm{m^2}$	permeability of liquid in porous medium
$K_{le}(= -K_{el})$ $\mathrm{kg \cdot m^{-3} \cdot s^{-1}}$	liquid-equiaxed momentum exchange coefficient
$K_{lc}(= K_{cl})$ $\mathrm{kg \cdot m^{-3} \cdot s^{-1}}$	liquid-columnar momentum exchange coefficient
$K_{ce}(= K_{ec})$ $\mathrm{kg \cdot m^{-3} \cdot s^{-1}}$	columnar-equiaxed momentum exchange coefficient
k 1	solute partitioning coefficient at the *l*/*s* interface
k_l, k_e, k_c $\mathrm{W \cdot m^{-1} \cdot K^{-1}}$	thermal conductivity
l m	actual columnar length in tip cell
l_{ref} m	reference length of control volume
$M_{le}(= -M_{el})$ $\mathrm{kg \cdot m^{-3} \cdot s^{-1}}$	liquid-equiaxed net mass-transfer rate
$M_{lc}(= -M_{cl})$ $\mathrm{kg \cdot m^{-3} \cdot s^{-1}}$	liquid-columnar net mass-transfer rate
$M_{ce}(= -M_{ec})$ $\mathrm{kg \cdot m^{-3} \cdot s^{-1}}$	columnar-equiaxed net mass-transfer rate
m K	slope of liquidus in phase diagram
m_E $\mathrm{m \cdot s^{-0.5}}$	slope of $x_{T_E} - \sqrt{t}$ curve
m_{tip} $\mathrm{m \cdot s^{-0.5}}$	slope of $x_{\mathrm{tip}} - \sqrt{t}$ curve
N_e $\mathrm{m^{-3} \cdot s^{-1}}$	equiaxed grain production rate by nucleation
n $\mathrm{m^{-3}}$	equiaxed grain number density
n' L	dimension index
n_c $\mathrm{m^{-3}}$	columnar trunk number density
$n_{\max}$ $\mathrm{m^{-3}}$	maximum equiaxed grain density, or maximum available nucleation sites in simultaneous nucleation law
p $\mathrm{N \cdot m^{-2}}$	pressure
p_0 $\mathrm{N \cdot m^{-2}}$	initial pressure
$Q_{le}(= -Q_{el})$ $\mathrm{J \cdot m^{-3} \cdot s^{-1}}$	total energy exchange between liquid and equiaxed phases
$Q_{le}^d(= -Q_{el}^d)$ $\mathrm{J \cdot m^{-3} \cdot s^{-1}}$	energy transfer between liquid and equiaxed phases
$Q_{le}^p(= -Q_{el}^p)$ $\mathrm{J \cdot m^{-3} \cdot s^{-1}}$	energy exchange due to phase change between liquid and equiaxed phases
$Q_{lc}(= -Q_{ec})$ $\mathrm{J \cdot m^{-3} \cdot s^{-1}}$	total energy exchange between liquid and columnar phases
$Q_{lc}^d(= -Q_{cl}^d)$ $\mathrm{J \cdot m^{-3} \cdot s^{-1}}$	energy transfer between liquid and columnar phases
$Q_{lc}^p(= -Q_{cl}^p)$ $\mathrm{J \cdot m^{-3} \cdot s^{-1}}$	energy exchange due to phase change between liquid and columnar phases
$Q_{ce}(= -Q_{ec})$ $\mathrm{J \cdot m^{-3} \cdot s^{-1}}$	total energy exchange between equiaxed and columnar phases
$Q_{ec}^d(= -Q_{ce}^d)$ $\mathrm{J \cdot m^{-3} \cdot s^{-1}}$	energy transfer between equiaxed and columnar phases
$Q_{ec}^p(= -Q_{ce}^p)$ $\mathrm{J \cdot m^{-3} \cdot s^{-1}}$	energy exchange due to phase change between equiaxed and columnar phases
Q_l^s, Q_e^s, Q_c^s $\mathrm{J \cdot m^{-3} \cdot s^{-1}}$	additional source terms in enthalpy equations
R m	radius component of the coordinate
$R(R_\mathrm{e}, R_\mathrm{c})$ m	grain radius (equiaxed, columnar)
R_f m	half of the columnar grain space
S_A $\mathrm{m^{-1}}$	surface area of columnar per volume
T_0 K	initial temperature
T, T_l, T_e, T_c K	temperature
T_E K	eutectic temperature
T_f K	melting point of pure metal (Fe)
T_{ref} K	reference temperature for enthalpy definition
ΔT K	constitutional undercooling
ΔT_N K	undercooling for maximum grain production rate
$\Delta T'_N$ K	undercooling needed in a simultaneous nucleation law
ΔT_{tip} K	undercooling at the columnar dendrite tip
ΔT_σ K	Gaussian distribution width of nucleation law
t S	time
Δt S	Time-step

$\mathbf{U}_{le}$ $(= -\mathbf{U}_{el})$ kg · m^{-2} · s^{-2}	total liquid-equiaxed momentum exchange rate
$\mathbf{U}_{le}^{d}(= -\,U_{el}^{d})$ kg · m^{-2} · s^{-2}	liquid-equiaxed momentum change due to drag force
$\mathbf{U}_{le}^{p}(= -\,U_{el}^{p})$ kg · m^{-2} · s^{-2}	liquid-equiaxed momentum exchange due to phase change
$\mathbf{U}_{lc}$ $(= -\mathbf{U}_{cl})$ kg · m^{-2} · s^{-2}	total liquid-columnar momentum exchange rate
$\mathbf{U}_{lc}^{d}(= -\,U_{cl}^{d})$ kg · m^{-2} · s^{-2}	liquid-columnar momentum change due to drag force
$\mathbf{U}_{lc}^{p}(= -\,U_{cl}^{p})$ kg · m^{-2} · s^{-2}	liquid-columnar momentum exchange due to phase change
$\mathbf{U}_{ce}$ $(= -\mathbf{U}_{ec})$ kg · m^{-2} · s^{-2}	total equiaxed-columnar momentum exchange rate
$\mathbf{U}_{ec}^{d}(= -\,U_{ec}^{d})$ kg · m^{-2} · s^{-2}	equiaxed-columnar momentum change due to drag force
$\mathbf{U}_{ce}^{p}(= -\,U_{ec}^{p})$ kg · m^{-2} · s^{-2}	equiaxed-columnar momentum exchange due to phase change
$\boldsymbol{u}_l$, $\boldsymbol{u}_e$, $\boldsymbol{u}_c$ m · s^{-1}	velocity component in x direction
$\boldsymbol{u}_l$, $\mathbf{u}_\mathrm{e}$, $\mathbf{u}_\mathrm{c}$ m · s^{-1}	velocity vector
$\Delta\boldsymbol{u}$ m · s^{-1}	relative velocity between melt and solid phases
V m · s^{-1}	growth velocity of unidirectional solidification
v_l, v_e, v_c m · s^{-1}	velocity component in y direction
v_R m · s^{-1}	grain growth speed in radius direction
v_tip M · s^{-1}	grain growth speed in tip direction
ΔV m^3	volume of the control volume element
$x_\mathrm{tip}, x_{T_L}, x_{T_E}$ m	distance of columnar tip front, liquidus, and eutectic isotherms from mold wall
β L	solidification shrinkage $(=(\rho_s - \rho_l)/\rho_s)$
β_T K^{-1}	thermal expansion coefficient
β_c L	solutal expansion coefficient
$\Delta\delta$ m	boundary mesh size
Γ m · K	Gibbs–Thomson coefficient
λ_1 M	columnar grain space
ρ_l, ρ_e, ρ_c, kg · m^{-3}	density
ρ_l^ref kg · m^{-3}	reference density
μ_l, μ_e kg · m^{-1} · s^{-1}	viscosity
μ_mix kg · m^{-1} · s^{-1}	mix viscosity
$\overline{\overline{\tau}}_l, \overline{\overline{\tau}}_e$ kg · m^{-1} · s^{-1}	stress-strain tensors

The subscripts *l, e,* and *c* indicate the liquid, equiaxed, and columnar phases.

ACKNOWLEDGMENTS

The authors acknowledge the excellent technical support of Dr. M. Pelzer and Dipl.-Ing. R. Postl, FLUENT/Germany.

REFERENCES

1. J.D. Hunt: *Mater. Sci. Eng.*, 1984, vol. 65, pp. 75-83.
2. P. Zhu and R.W. Smith: *Acta Metall. Mater.*, 1992, vol. 40, pp. 683-92.
3. Ch.-A. Gandin, T. Jalanti, and M. Rappaz: in *Modeling of Casting, Welding and Advanced Solidification Processes VIII,* B.G. Thomas and C. Beckermann, eds., TMS, Warrendale, PA, 1998, pp. 363-74.
4. C.Y. Wang and C. Beckermann: *Metall. Mater. Trans. A*, 1994, vol. 25A, pp. 1081-93.
5. M.A. Martorano, C. Beckermann, and C.-A. Gandin: *Metall. Mater. Trans. A*, 2003, vol. 34A, pp. 1657-74.
6. A. Ohno: *Solidification—The Separation Theory and Its Practical Applications*, Springer-Verlag, Berlin, 1987, pp. 1-123.
7. A. Ludwig and M. Wu: *Metall. Mater. Trans. A*, 2002, vol. 33A, pp. 3673-83.
8. M. Wu, A. Ludwig, A. Bührig-Polaczek, M. Fehlbier, and P.R. Sahm: *Int. J. Heat Mass Transfer*, 2003, vol. 46, pp. 2819-32.
9. M. Rappaz: *Int. Mater. Rev.*, 1989, vol. 34, pp. 93-123.
10. *Fluent 6.1 User's Guide,* vol. 4, Fluent Inc., Lebanon, NH, 2003.
11. W. Kurz and D.J. Fisher: *Fundamentals of Solidification*, Trans Tech Publications, Aedemannsdorf, Switzerland, 1989, pp. 65-89.
12. J. Lipton, M.E. Glicksman, and W. Kurz: *Mater. Sci. Eng.*, 1984, vol. 65, pp. 57-63.
13. J.P. Gu and C. Beckermann: *Metall. Mater. Trans. A*, 1999, vol. 30A, pp. 1357-66.
14. M. Schneider and C. Beckermann: *Int. J. Heat Mass Transfer*, 1995, vol. 38, pp. 3455-73.
15. H. Jacobi and K. Schwerdtfeger: *Metall. Trans. A*, 1976, vol. 7A, pp. 811-20.
16. M.C. Flemings and G.E. Nereo: *Trans. TMS-AIME*, 1967, vol. 239, pp. 1449-61.
17. M.C. Flemings, R. Mehrabian, and G.E. Nereo: *Trans. TMS-AIME*, 1968, vol. 242, pp. 41-49.
18. H. Kato and J.R. Cahoon: *Metall. Trans. A*, 1985, vol. 16A, pp. 579-87.
19. Ch.-A. Gandin and M. Rappaz: *Acta Metall. Mater.*, 1994, vol. 42, pp. 2233-46.
20. M. Rappaz and C.A. Gandin: *Acta Metall. Mater.*, 1993, vol. 41, pp. 345-60.
21. S.C. Flood and J.D. Hunt: *Metals Handbook—Castings*, 9th ed., ASM INTERNATIONAL, Metals Park, OH, 1998, vol. 15, pp. 130-36.
22. J. Campbell: *Castings*, Butterworth Heinemann Ltd., Oxford, United Kingdom, 1991, pp. 151-58.
23. A. Ludwig and M. Wu: *Solidification Processes and Microstructures: Symp. in Honor of Wilfried Kurz*, M. Rappaz *et al.*, eds., TMS, Warrendale, PA, 2004, pp. 99-110.
24. M. Wu, A. Ludwig, and J. Luo: *Mater. Sci. Forum*, 2005, vol. 475–479, pp. 2725-30.
25. M. Wu and A. Ludwig: *Adv. Eng. Mater.*, 2003, vol. 5, pp. 62-66.
26. M.C. Flemings: *Solidification Processes*, McGraw-Hill, New York, NY, 1974.
27. I. Ohnaka: *Metals Handbook—Castings*, 9th ed., ASM INTERNATIONAL, Metals Park, OH, 1998, vol. 15, pp. 136-41.
28. Y. Nakagawa and A. Momose: *Tetsu-to-Hagané*, 1967, vol. 53, pp. 1477-508.
29. C. Beckermann and R. Viskanta: *Appl. Mech. Rev.*, 1993, vol. 46, pp. 1-27.
30. C. Beckermann: *Int. Mater. Rev.*, 2002, vol. 47, pp. 243-61.
31. O. Nielsen, A. Appolaire, H. Combeau, and A. Mo: *Metall. Mater. Trans. A*, 2001, vol. 32A, pp. 2049-60.
32. F.P. Incropera and D.P. Dewitt: *Fundamentals of Heat and Mass Transfer*, 5th ed., John Wiley & Sons, Inc., New York, NY, 2002.
33. J. Guo and C. Beckermann: *Num. Heat Transfer*, 2003, vol. 44, pp. 559-76.